The Astrophysical Journal, 1003:151 (21pp), 2026 June 1 https://doi.org/10.3847/1538-4357/ae5dc2

Joint X-Ray, Kinetic Sunyaev–Zeldovich, and Weak Lensing Measurements: Toward a Consensus Picture of Efficient Gas Expulsion from Groups and Clusters

Jared C. Siegel[1,8], Alexandra Amon[1], Ian G. McCarthy[2], Leah Bigwood[3,4], Masaya Yamamoto[1], Esra Bulbul[5], Jenny E. Greene[1], Jamie McCullough[1], Matthieu Schaller[6,7], and Joop Schaye[7]
[1] Department of Astrophysical Sciences, Princeton University, 4 Ivy Lane, Princeton, NJ 08544, USA; siegeljc@princeton.edu
[2] Astrophysics Research Institute, Liverpool John Moores University, Liverpool, L3 5RF, UK
[3] Institute of Astronomy and Kavli Institute for Cosmology, University of Cambridge, Madingley Road, Cambridge, CB3 0HA, UK
[4] Kavli Institute for Cosmology (KICC), University of Cambridge, Madingley Road, Cambridge CB3 0HA, UK
[5] Max Planck Institute for Extraterrestrial Physics, Giessenbachstrasse 1, 85748 Garching, Germany
[6] Lorentz Institute for Theoretical Physics, Leiden University, PO box 9506, 2300 RA Leiden, The Netherlands
[7] Leiden Observatory, Leiden University, PO Box 9513, 2300 RA Leiden, The Netherlands
Received 2025 October 7; revised 2026 March 22; accepted 2026 April 8; published 2026 May 21

Abstract

There is no consensus on how baryon feedback shapes the underlying matter distribution from either simulations or observations. We confront the uncertain landscape by jointly analyzing new measurements of the gas distribution around groups and clusters—DESI+ACT kinetic Sunyaev–Zel'dovich (kSZ) effect profiles and eROSITA X-ray gas masses—with mean halo masses characterized by galaxy–galaxy lensing. Across a wide range of halo masses ($M_{500} = 10^{13-14} M_{\odot}$) and redshifts ($0 < z < 1$), we find evidence of more efficient gas expulsion beyond several R_{500} than predicted by most state-of-the-art simulations. A like-with-like comparison reveals all kSZ and X-ray observations are inconsistent with the fiducial 1 Gpc^3 hydrodynamical FLAMINGO simulation, which was calibrated to reproduce pre-eROSITA X-ray gas fractions: eROSITA X-ray gas fractions are 2 × lower than the simulation, and the kSZ measurements are combined $>8\sigma$ discrepant. The FLAMINGO simulation variant with the most gas expulsion, and therefore the most suppression of the matter power spectrum relative to a dark-matter-only simulation, provides a good description of how much gas is expelled and how far it extends; the enhanced gas depletion is achieved by more powerful but less frequent AGN outbursts. Joint kSZ, X-ray, and lensing measurements form a consistent picture of gas expulsion beyond several R_{500}, implying a more suppressed matter power spectrum than predicted by most recent simulations. Complementary observables (e.g., thermal Sunyaev–Zel'dovich effect and fast radio bursts) and next-generation simulations are critical to understanding the physical mechanism behind this extreme gas expulsion and mapping its impact on the large-scale matter distribution.

Unified Astronomy Thesaurus concepts: Weak gravitational lensing (1797); Large-scale structure of the universe (902); Galaxy formation (595)

1. Introduction

Baryon feedback redistributes gas relative to the underlying dark matter distribution. Active galactic nuclei (AGNs), supernova, and stellar winds all heat and expel gas from halos, while cooling incites halo contraction. For massive galaxies ($\gtrsim L^{\star}$), AGNs are the dominant feedback mechanism. AGN feedback was originally motivated by the observed coevolution of supermassive black holes with their host galaxies (e.g., J. Silk & M. J. Rees 1998; V. Springel et al. 2005; J. Kormendy & L. C. Ho 2013; T. M. Heckman & P. N. Best 2014). For groups and clusters, energy injection by AGNs prevents efficient cooling of the gas reservoir (e.g., B. R. McNamara & P. E. J. Nulsen 2007; C. Conroy & J. P. Ostriker 2008; I. G. McCarthy et al. 2011; A. C. Fabian 2012; M. Gitti et al. 2012; M. Gaspari et al. 2020; D. Eckert et al. 2021). On Mpc scales ($k > 0.1\,h\,\mathrm{Mpc}^{-1}$), there is now mounting evidence that gas expulsion impacts the large-scale matter distribution (L. Bigwood et al. 2024; S. Grandis et al. 2024a; M. Kovač et al. 2025; N. Dalal et al. 2026). In this paper, we jointly study three measures of the matter distribution—the kinetic Sunyaev–Zel'dovich (kSZ) effect, X-ray cluster gas mass fractions, and galaxy–galaxy lensing (GGL)—to constrain the impact of feedback as a function of radius, halo mass, and redshift.

How gas is redistributed by feedback on large scales is a fundamental question in galaxy evolution and a critical ingredient for large-scale structure cosmology. Modeling the matter distribution on small scales ($k > 0.1\,h\,\mathrm{Mpc}^{-1}$) requires knowledge of how baryon feedback suppresses the matter power spectrum relative to a dark-matter-only universe (e.g., N. E. Chisari et al. 2019). By constraining how much gas is depleted from halos and how far it is expelled, observations of the gas distribution place powerful constraints on the suppression of the matter power spectrum. Power suppression was first constrained with X-ray observations of the intracluster medium (ICM) in groups and clusters. The baryon fraction is found to increase as a function of radius and halo mass, returning to the universal baryon fraction at large radii of massive clusters (M. Sun et al. 2009; G. E. Bulbul et al. 2012; A. J. R. Sanderson et al. 2013; L. Lovisari et al. 2015; D. Eckert et al. 2016, 2019). By more efficiently expelling gas

[8] NSF Graduate Research Fellow.

beyond R_{500}, stronger feedback processes are expected to lower the typical gas fraction at a given halo mass. Prior studies have inferred moderate power suppression ($\sim$2% at $k = 1\,h$ Mpc^{-1}) by either calibrating cosmological hydrodynamical simulations to X-ray measurements (e.g., M. P. van Daalen et al. 2011; I. G. McCarthy et al. 2017; N. A. Henden et al. 2018; M. P. van Daalen et al. 2020; J. Salcido et al. 2023; J. Schaye et al. 2023) or by semianalytic modeling (e.g., S. N. B. Debackere et al. 2020; S. K. Giri & A. Schneider 2021; L. Bigwood et al. 2024; S. Grandis et al. 2024a; M. Kovač et al. 2025).

More recently, evidence has emerged from a range of observables that power suppression is more extreme than most simulations predict: $\sim$10% at $k = 1\,h$ Mpc^{-1}; power suppression has been inferred from modeling of the observations (A. Amon & G. Efstathiou 2022; A. Schneider et al. 2022; C. Preston et al. 2023; L. Bigwood et al. 2024; M. Kovač et al. 2025; R. Reischke & S. Hagstotz 2025; N. Dalal et al. 2026) and by comparison to simulations (B. Hadzhiyska et al. 2025a, 2025b; I. G. McCarthy et al. 2025; B. Ried Guachalla et al. 2025). Stacked measurements of the kSZ effect from DESI+ACT have been critical to this work (B. Hadzhiyska et al. 2025b; B. Ried Guachalla et al. 2025); after rapid development over the past decade (E. Schaan et al. 2016; N. Battaglia et al. 2017; E. Schaan et al. 2021; M. Mallaby-Kay et al. 2023), kSZ measurements now offer powerful constraints on the gas content of groups beyond several R_{500}.

The latest X-ray measurements also favor strong power suppression. The first release of the eROSITA all-sky X-ray survey reports lower average gas fractions than previously observed at a given halo mass (A. Liu et al. 2022; E. Bulbul et al. 2024), potentially highlighting the impact of selection effects on prior samples (R. Seppi et al. 2022; I. Marini et al. 2024). Stacking of eROSITA images on optically selected groups also yields systematically lower gas fractions (P. Popesso et al. 2024b).

To address the uncertain observational landscape, we adopt a multiprobe view of feedback. This paper provides the first joint analysis across kSZ, X-ray, and GGL to constrain the gas distribution across a wide range of radial scales, halo masses, and redshifts: X-ray gas fractions probe the low-redshift cluster mass regime, while kSZ measurements extend to higher redshifts and lower masses. We consider gas mass measurements from the first release of the eROSITA all-sky survey (E. Bulbul et al. 2024) and kSZ effect profiles from the Sloan Digital Sky Survey (SDSS) and the Atacama Cosmology Telescope (ACT; E. Schaan et al. 2021) and DESI+ACT (B. Ried Guachalla et al. 2025), described in Section 2, in comparison to the 1 Gpc^3 FLAMINGO hydrodynamical simulations (J. Schaye et al. 2023; R. Kugel et al. 2023), which we summarize in Section 3. We produce new GGL measurements using overlapping weak-lensing data from the Dark Energy Survey (DES), the Kilo-Degree Survey (KiDS), and the Hyper Suprime-Camera (HSC) Survey (M. Gatti et al. 2021; B. Giblin et al. 2021; X. Li et al. 2022) to measure the mean halo masses of the X-ray and kSZ samples. As described in Section 4, this resolves two key uncertainties in interpreting these samples—the halo mass and the satellite fraction, which are degenerate with the inferred magnitude of gas expulsion—and enables a like-with-like comparison to the simulations (I. G. McCarthy et al. 2025). We present our simulation comparison in Section 5 and discuss our findings on the magnitude of matter power suppression in Section 6. We conclude in Section 7.

2. Observations

2.1. kSZ Effect Profiles

Cosmic microwave background (CMB) photons inverse Compton scatter off the intervening ionized gas around galaxies and clusters. Due to the bulk motion and velocity dispersion of the gas, these interactions impart a Doppler shift to the CMB photons: the kSZ (R. A. Sunyaev & Y. B. Zeldovich 1980) and thermal Sunyaev–Zel'dovich (tSZ; R. A. Sunyaev & Y. B. Zeldovich 1972) effects, respectively. The kSZ effect is proportional to the electron number density and the peculiar velocity of the gas, while the tSZ effect depends on the electron pressure (integrated along the line of sight). By measuring the kSZ effect as a velocity weighted stack, contamination from the cosmic infrared background, which is uncorrelated with the velocity field, cancels on average; the tSZ effect is relatively more sensitive to contamination (e.g., R. H. Liu et al. 2025).

The kSZ effect manifests as a temperature fluctuation in the CMB (e.g., E. Schaan et al. 2021):

$$\frac{\Delta T_{\rm kSZ}(\boldsymbol{\theta})}{T_{\rm CMB}} = -\sigma_{\rm T} \int n_e(\boldsymbol{\theta}, z) \frac{v_{e,\rm r}(\boldsymbol{\theta}, z)}{c} e^{-\tau(\boldsymbol{\theta},z)} \frac{d\chi}{1+z}, \quad (1)$$

where $\boldsymbol{\theta}$ is an angular position on the sky, $\sigma_{\rm T}$ is the Thomson scattering cross-section, c is the speed of light, $n_e(\boldsymbol{\theta}, z)$ is the electron density, $v_{e,\rm r}(\boldsymbol{\theta}, z)$ is the electron velocity along the line of sight, and χ is the comoving radial distance. The optical depth to Thompson scattering between the observer and redshift z is

$$\tau(\boldsymbol{\theta}, z) = \sigma_{\rm T} \int n_e(\boldsymbol{\theta}, z) \frac{d\chi}{1+z}. \quad (2)$$

The gas of interest is optically thin, therefore, for one galaxy

$$\frac{\Delta T_{\rm kSZ}}{T_{\rm CMB}} \approx -\tau_{\rm gal} \frac{v_{e,\rm r,gal}}{c}. \quad (3)$$

The kSZ signal must be stacked across many galaxies to achieve a high signal-to-noise ratio measurement (E. Schaan et al. 2021).

In this work, we adopt the stacked kSZ effect profiles of E. Schaan et al. (2021) and B. Ried Guachalla et al. (2025), which used spectroscopic redshift tracers from SDSS and DESI, respectively; we also consider the measurements of B. Hadzhiyska et al. (2025b) in Appendix C, which used photometric redshifts for the velocity reconstruction. The CMB temperature maps and galaxy samples underlying these measurements are described in Sections 2.1.1 and 2.1.2, respectively.

The stacked measurements use compensated aperture photometry (CAP) filters. For a galaxy located at $\boldsymbol{\theta}$ on the sky, CAP filtering measures the cumulative kSZ effect profile as a function of angular separation from the galaxy θ_d:

$$\mathcal{T}(\theta_d) = \int d^2\theta \Delta T_{\rm kSZ}(\theta) W_{\theta_d}(\theta), \quad (4)$$

$$W_{\theta_d}(\theta) = \begin{cases} 1 & \text{if } \theta < \theta_d \\ -1 & \text{if } \theta_d \leqslant \theta \leqslant \sqrt{2}\,\theta_d, \\ 0 & \text{if } \theta > \sqrt{2}\,\theta_d \end{cases} \quad (5)$$

i.e., the temperature fluctuation within θ_d of the galaxy is summed and then background subtracted by the temperature fluctuations outside θ_d.

Since the kSZ effect is proportional to the velocity of the gas, simply stacking $\mathcal{T}(\theta_d)$ from many galaxies would result in a null signal; galaxies' peculiar velocities are equally likely to be positive or negative. The stacked kSZ signal is therefore measured by a combination of velocity and inverse-variance weighting (E. Schaan et al. 2021; B. Ried Guachalla et al. 2025):

$$\hat{T}_{\rm kSZ}(\theta_d) = -\frac{1}{r_{v,\rm bias}} \frac{v_{\rm rec}^{\rm rms}}{c} \frac{\sum_i \mathcal{T}_i(\theta_d)\left(\frac{v_{i,\rm rec}}{c}\right)\sigma_i^{-2}}{\sum_i \left(\frac{v_{i,\rm rec}}{c}\right)^2 \sigma_i^{-2}}, \quad (6)$$

where $v_{i,\rm rec}$ is the estimated line-of-sight peculiar velocity for the ith galaxy, $v_{\rm rec}^{\rm rms}$ is the standard deviation of the reconstructed peculiar velocities, and σ_i^2 is the variance in $\mathcal{T}_i(\theta_d)$. To account for biases in the peculiar velocity reconstruction, the stacked kSZ signal is divided by the correlation between the true and reconstructed velocities in mock catalogs:

$$r_{v,\rm bias} = \frac{\langle v_{\rm true}\, v_{\rm rec}\rangle}{v_{\rm true}^{\rm rms}\, v_{\rm rec}^{\rm rms}}. \quad (7)$$

2.1.1. SDSS BOSS: LOWZ and CMASS

E. Schaan et al. (2021) measured the kSZ effect profiles for two galaxy samples (LOWZ and CMASS) from the Baryon Oscillation Spectroscopic Survey (BOSS) DR10 release (C. P. Ahn et al. 2014) using the DR5 CMB temperature maps of ACT (J. W. Fowler et al. 2007; D. S. Swetz et al. 2011; S. W. Henderson et al. 2016; R. J. Thornton et al. 2016) and Planck (Planck Collaboration et al. 2020). E. Schaan et al. (2021) considered the 90 and 150 GHz frequency ACT maps. We adopt the results derived from the 150 GHz temperature map due to the higher signal-to-noise ratio and higher-resolution beam ($1.'3$ compared to $2.'1$ for 90 GHz).

The LOWZ ("low-redshift") sample includes red galaxies between $0.15 < z < 0.4$. The CMASS ("constant mass") sample targets massive galaxies in the redshift range $0.4 < z < 0.8$ (C. P. Ahn et al. 2012). To avoid contamination by the tSZ signal of massive halos, the few thousand most massive galaxies are omitted, resulting in approximately 140,000 and 350,000 galaxies for LOWZ and CMASS, respectively; E. Schaan et al. (2021) rejected $M_{\rm virial} > 10^{14}\,M_\odot$ halos using the stellar to halo mass relation of A. V. Kravtsov et al. (2018). By comparing the true and recovered velocities in mock BOSS catalogs (M. Manera et al. 2013, 2015), E. Schaan et al. (2021) derived a peculiar velocity bias factor of $r_{\rm v} = 0.7$.

2.1.2. DESI: BGS and LRG

We consider the B. Ried Guachalla et al. (2025) kSZ effect profiles for two samples of galaxies from DESI DR1: the Bright Galaxy Survey (BGS; C. Hahn et al. 2023) and the Luminous Red Galaxy sample (LRG; R. Zhou et al. 2023a). CMB temperature fluctuations are measured from the ACT DR6 (S. Naess et al. 2025) and Planck (Planck Collaboration et al. 2020) maps. To mitigate tSZ contamination, B. Ried Guachalla et al. (2025) masked temperature outliers in the ACT map.

The BGS sample is magnitude limited and spans $0 < z < 0.6$. Following A. G. Adame et al. (2025a), B. Ried Guachalla et al. (2025) limited the BGS sample to $0.1 < z < 0.4$ and applied a luminosity selection as a function of redshift, to create a sample with an approximately constant number density. The BGS kSZ stack consists of 96,000 galaxies. For this sample, B. Ried Guachalla et al. (2025) adopted the peculiar velocities of A. G. Adame et al. (2025b) and set the reconstruction bias to $r_{\rm v} = 0.64$, with an estimated 3% uncertainty (B. Hadzhiyska et al. 2024). For the current measurements, the reported uncertainties on the velocity reconstruction are negligible.

The LRG sample consists of massive quenched galaxies between $0.4 < z < 1.1$. B. Ried Guachalla et al. (2025) divided the LRG sample into four stellar mass bins: $\log_{10} M_\star/M_\odot =$ (10.5, 11.2), (11.2, 11.4), (11.4, 11.6), and (11.6, 12.5). The mass selection is performed on stellar masses from R. Zhou et al. (2023a), which are derived from DESI Legacy Imaging photometry via a random forest algorithm trained on the Stripe 82 Massive Galaxy Catalog (K. Bundy et al. 2015). B. Ried Guachalla et al. (2025) set the peculiar velocity reconstruction bias for the LRGs to $r_v = 0.65$, with an estimated 2% uncertainty (B. Hadzhiyska et al. 2024).

B. Ried Guachalla et al. (2025) used the harmonic-space Internal Linear Combination (hILC) CMB temperature map, which combines the multiple ACT DR6 channels (90, 150, and 220 GHz) with Planck (W. Coulton et al. 2024), unlike E. Schaan et al. (2021), where the kSZ effect profiles were measured separately for the ACT channels. Before combining the individual frequency maps, each is convolved with a Gaussian beam ($1.'6$ FWHM).

We also consider the DESI+ACT kSZ measurements of B. Hadzhiyska et al. (2025b), which use the photometric sample of LRG from the DESI Legacy Imaging Survey. B. Hadzhiyska et al. (2025b) adopted the photometric redshifts of R. Zhou et al. (2023b) and used the same ACT+Planck CMB temperature map, velocity reconstruction pipeline (D. J. Eisenstein et al. 2007; M. White 2015), and stellar mass estimates (R. Zhou et al. 2023a) as B. Ried Guachalla et al. (2025). B. Hadzhiyska et al. (2025b) measured the kSZ effect profile for four bins of stellar mass using the Main LRG sample: $\log_{10} M_*/M_\odot =$ (11, 11.25), (11.25, 11.5), (11.5, 12), and (12, 13.5); we omit the highest mass bin because of its small sample size (<3000 galaxies) and potential tSZ contamination.

In this work, we analyze the spectroscopic measurements for our fiducial study and present a full investigation of the photometric measurements in Appendix C.

2.2. eROSITA X-Ray Gas Mass Fractions

The extended ROentgen Survey with an Imaging Telescope Array (eROSITA) satellite (P. Predehl et al. 2021), a soft X-ray telescope on board the Spectrum–Roentgen–Gamma observatory (R. Sunyaev et al. 2021), provides comprehensive X-ray data for a large and well-defined sample of thousands of galaxy groups and clusters in the Western Galactic Hemisphere. The first eROSITA All-Sky Survey catalog (eRASS1) includes more than 12,000 optically confirmed

X-ray groups and clusters between the local Universe and $z \approx 1.3$ (E. Bulbul et al. 2024; M. Kluge et al. 2024) selected from the 1,300,000 total eROSITA X-ray detections (A. Merloni et al. 2024). The eRASS1 groups and clusters are X-ray detected and optically confirmed with the `eROMaPPer` algorithm (E. S. Rykoff et al. 2014, 2016; M. Kluge et al. 2024). Photometric redshifts are adopted from `eROMaPPer` and spectroscopic redshifts, where available. The reported photometric redshift accuracy is $\delta z/(1+z) \lesssim 0.005$ for $0.05 < z < 0.9$ (M. Kluge et al. 2024).

Gas density profiles are derived by fitting a parametric model to the X-ray images using the MBProj2D software, following convolution of surface brightness with the temperature of the ICM through a forward modeling approach (J. S. Sanders et al. 2018; A. Liu et al. 2022; E. Bulbul et al. 2024). The gas mass is then calculated by integrating the volume density. Total halo masses M_{500} are estimated from a weak-lensing calibrated scaling relation between redshift, X-ray count rate, and shear. The scaling relation is calibrated using 2533 clusters in the common area of eROSITA with weak-lensing surveys; the calibration clusters are drawn from the higher fidelity "cosmology" sample of 5249 clusters between $0.1 < z < 0.8$ (E. Bulbul et al. 2024). The mass estimates include corrections for miscentering and cluster member contamination, as well as calibration from forward modeling of simulated shear profiles (S. Grandis et al. 2024b; F. Kleinebreil et al. 2025; N. Okabe et al. 2025).

To validate the reported halo masses, we measure the GGL profile for bins of eROSITA clusters. We define four samples of clusters: $\log_{10} M_{500}/M_\odot = (13.3, 14.0)$ and $(14.0, 14.5)$ between $0.05 < z < 0.1$, and $\log_{10} M_{500}/M_\odot = (13.5, 14.0)$ and $(14.0, 14.5)$ between $0.1 < z < 0.2$. The higher-redshift bins coincide with the redshift range used for the eROSITA weak-lensing mass calibration, whereas the lower redshift bins explore a redshift and mass range not previously calibrated.

3. FLAMINGO Simulations

The FLAMINGO simulation suite includes 16 hydrodynamical simulations of varied resolution, box size, subgrid modeling, and cosmology (J. Schaye et al. 2023). We consider the 1 Gpc^3 intermediate-resolution simulations ($m_{\rm gas} = 1.09 \times 10^9\, M_\odot$), with 2×1800^3 gas and dark matter particles and 1000^3 neutrino particles. These simulations adopt the maximum likelihood cosmological parameters of the DES Y3 "3×2pt + All Ext." flat ΛCDM cosmology (T. M. C. Abbott et al. 2022). The simulations successfully reproduce the galaxy stellar mass function, the central black hole–stellar mass relation, the cosmic star formation rate density, and cluster scaling relations (J. Schaye et al. 2023; J. Braspenning et al. 2024).

For the fiducial simulation, the subgrid physics (e.g., star formation, stellar evolution, radiative cooling, and AGNs) were calibrated to reproduce the observed $z = 0$ stellar-to-halo-mass relation and the gas fractions of groups and clusters (R. Kugel et al. 2023). The gas fraction data was assembled from a collection of pre-eROSITA surveys, including A. Vikhlinin et al. (2006), B. J. Maughan et al. (2008), J. Rasmussen & T. J. Ponman (2009), M. Sun et al. (2009), G. W. Pratt et al. (2010), Y.-T. Lin et al. (2012), T. F. Laganá et al. (2013), A. J. R. Sanderson et al. (2013), A. H. Gonzalez et al. (2013), L. Lovisari et al. (2015), H. Hoekstra et al. (2015), R. J. Pearson et al. (2017), S. L. Mulroy et al. (2019), L. Lovisari et al. (2020), and D. Akino et al. (2022); note that with the exception of D. Akino et al. (2022), selection effects were not accounted for. Variants with stronger (weaker) baryon feedback were produced by calibrating to gas fraction measurements shifted down (up) by $N\sigma$, where σ is the observational uncertainty on the mean gas fraction relation and $N \in [2, 4, 8]$. The feedback variants were still calibrated to the observed stellar to halo mass relation.

The strength of baryon feedback is primarily regulated by the AGN subgrid model. Observationally, AGNs are found to couple to the surrounding gas through either the jet or radiative modes (E. Choi et al. 2012); the jet mode is dominant in the most massive black holes and transfers momentum to the gas via collimated outflows, while the radiative mode deposits thermal energy to neighboring gas (T. M. Heckman & P. N. Best 2014). The fiducial FLAMINGO simulation assumes only radiative AGN feedback, following C. M. Booth & J. Schaye (2009). As a black hole grows, a fraction of the accreted rest-mass energy heats the neighboring gas; the fraction of energy converted into heat is $\epsilon_{\rm r}\epsilon_{\rm f} = 0.015$, where $\epsilon_{\rm r} = 0.1$ is the radiative efficiency and $\epsilon_{\rm f} = 0.15$ is the fraction of the radiated energy that heats the gas. Due to the large masses of gas particles, releasing the heat from the AGN each time step causes numerical overcooling (C. Dalla Vecchia & J. Schaye 2012). Instead, the feedback energy is stored internally until it can heat the nearest gas particle by $\Delta T_{\rm AGN}$. Increasing $\Delta T_{\rm AGN}$ corresponds to more powerful but less-frequent AGN outbursts, resulting in stronger baryon feedback. The FLAMINGO suite also includes two simulations with jet mode AGN feedback following F. Huško et al. (2022). The jet variants were only produced for a limited range of feedback strengths (the fiducial gas fractions and -4σ), unlike the radiative mode variants, which extend to -8σ.

In this paper, we study four FLAMINGO simulations: fiducial radiative feedback (L1_m9), stronger radiative feedback ($f_{\rm gas} - 4\sigma$), stronger jet feedback (Jet_$f_{\rm gas} - 4\sigma$), and strongest radiative feedback ($f_{\rm gas} - 8\sigma$).

4. Characterizing the Galaxy Samples

Measurements of the stacked kSZ effect and X-ray gas mass fractions are sensitive to the redshift and halo mass of the underlying sample, in addition to feedback strength. A careful selection of simulated galaxies is critical to comparing kSZ and X-ray observations with simulations: Figure 1 (top panel) shows simulated profiles of the kSZ effect from the FLAMINGO simulations for a range of redshifts (left), halo masses (middle), and feedback strengths (right). Even when the kSZ profile amplitudes are normalized (bottom panels), the changes in the shape of the predicted kSZ signal with redshift and halo mass are degenerate with variations in feedback strength; because the stacked kSZ effect profiles are effectively enclosed gas profiles, we normalize the profiles to the largest radial bin. As a result, mismatches in the mean halo mass or redshift between the observed and simulated samples can bias the inferred feedback strength (bottom panel of Figure 1). Likewise, the enclosed hot gas mass inferred from X-ray observations is expected to vary with the redshift and halo mass of the sample (J. Braspenning et al. 2024). This poses a challenge, because selecting a simulated galaxy sample with the same halo mass as an observed sample is nontrivial.

Following I. G. McCarthy et al. (2025), we ensure that the simulated galaxy samples have the same mean halo mass as the observations using GGL: for a given observable, we select

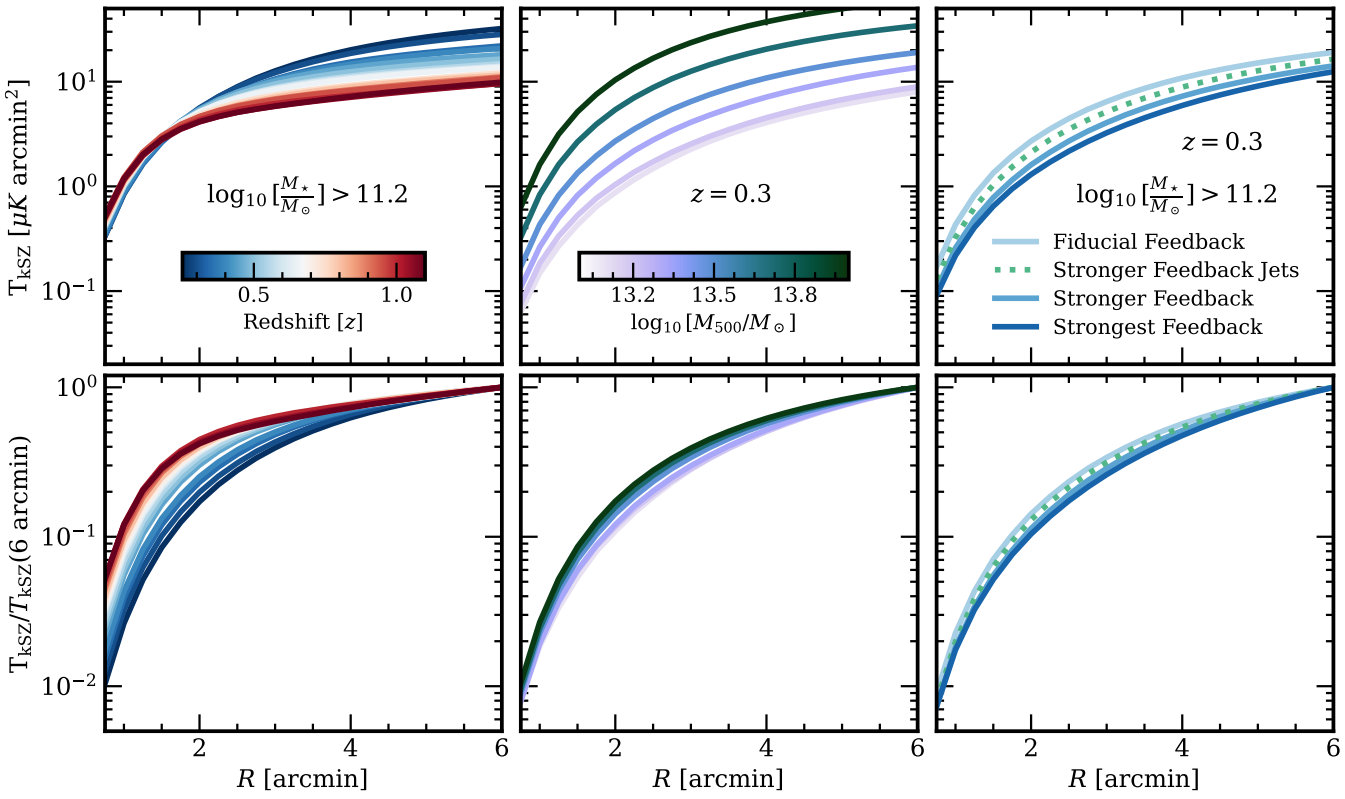

Figure 1. Simulated kSZ effect profiles from FLAMINGO for a range of redshifts (left), halo masses (center), and feedback strengths (right). For each kSZ stack, we select simulated halos by a minimum stellar mass cut. For the left and center panels, we present the kSZ effect from the fiducial FLAMINGO simulation. On the right, we compare four FLAMINGO simulations of varying feedback strength at a fixed redshift and minimum stellar mass selection. The bottom row highlights the challenge of inferring feedback strength from the shape of the profile alone: changes in feedback strength are degenerate with the mean redshift and mass of the sample, even when the amplitudes of the kSZ profiles are normalized.

galaxies from the simulation such that their stacked GGL profile is consistent with the measured lensing profile.

4.1. Galaxy–Galaxy Lensing

Light from distant background galaxies (sources) is tangentially sheared by foreground structures (lenses), known as GGL. We use GGL to infer the total mass profiles of the SDSS and DESI kSZ samples and the eROSITA X-ray samples, forming the basis of our like-with-like comparisons with the FLAMINGO simulations.

For a foreground lens at redshift z_l and comoving distance χ_l, the induced tangential shear on a background source at angular separation θ from the lens is

$$\gamma_t(R = \theta\chi_l) = \frac{\Delta\Sigma(R)}{\Sigma_{crit}}, \tag{8}$$

where $\Delta\Sigma(R) = \bar{\Sigma}(<R) - \Sigma(R)$ is the excess surface density: the difference between the average surface density within R and the projected surface density at radius R. Σ_{crit} is the comoving critical surface mass density

$$\Sigma_{crit}^{-1} = \frac{4\pi G}{c^2}\frac{D_l D_{ls}}{D_s}(1 + z_l)^2, \tag{9}$$

where D_l and D_s are the angular diameter distances to the lens and source, respectively, and $D_{ls} = D_s - D_l$.

We measure GGL through a weighted cross-correlation of the shapes of background sources ϵ with the positions of foreground lenses. At a given angular separation θ between lens and source pairs, the tangential shear estimator is

$$\langle\gamma_t(\theta)\rangle = \frac{\sum_{ls}\epsilon_t w_{ls}}{\sum_{ls} w_{ls}}, \tag{10}$$

where the summation is over all lens–source pairs separated by an angular separation of θ, ϵ_t is the tangential ellipticity component of each source, and w_{ls} is the combined weight of each lens–source pair. Considering an ensemble of source galaxies with a calibrated redshift probability distribution, $n(z_s)$, the average comoving critical surface density is

$$\bar{\Sigma}_{crit}^{-1}(z_l) = \frac{4\pi G(1 + z_l)^2}{c^2}\int dz_s n(z_s)\frac{D_l D_{ls}}{D_s}. \tag{11}$$

The average excess surface mass density is then

$$\Delta\Sigma(R) = \frac{\sum_{ls}\epsilon_t w_{ls}}{\sum_{ls}\bar{\Sigma}_{crit}^{-1}(z_l) w_{ls}}. \tag{12}$$

The comoving $\Delta\Sigma(R)$ measurements for the DESI kSZ and eROSITA X-ray samples are presented in Figures 2 and 3, respectively. For the DESI lenses, we apply the same ACT mask and use the same stellar mass estimates (R. Zhou et al. 2023a) as in B. Ried Guachalla et al. (2025). The GGL signals are measured with `dsigma` (J. Lange & S. Huang 2022) using the DES Y3, KiDS 1000, and HSC Y3 shear catalogs. The covariance matrix for each measurement is estimated with a leave-one-out Jackknife process (Appendix A). For the SDSS kSZ samples, we adopt the GGL measurements of A. Amon et al. (2023). In Appendix A, we detail the methodology for

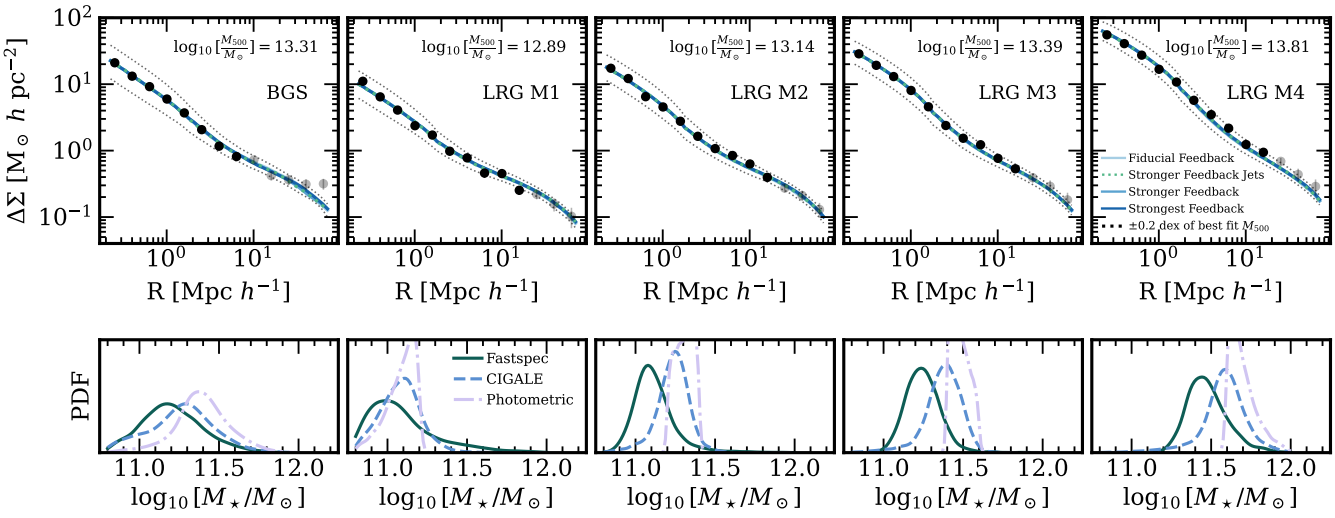

Figure 2. Top panels: the measured GGL profiles (black) of the DESI kSZ samples, alongside the best-fitting FLAMINGO $\Delta\Sigma$ profiles from the four simulations we consider. The FLAMINGO GGL profiles are calculated by stacking all simulated galaxies above a minimum stellar mass. At the top of each panel, we report the mean halo mass for the best-fitting selection of simulated galaxies from the fiducial FLAMINGO simulation. The dotted lines represent the $\Delta\Sigma$ profile for halo masses ±0.2 dex of the best fit. Tangential separations larger than the size of the Jackknife regions (light gray) are omitted from our analysis (Appendix A). Bottom panels: the stellar mass distributions of the DESI samples as measured by `FastSpecFit`, `CIGALE`, and the photometric random forest of R. Zhou et al. (2023a); note that B. Ried Guachalla et al. (2025) defined the LRG mass bins using the photometric estimates.

computing these measurements, including corrections for known systematics. We demonstrate the robustness of the signals to survey choice, contamination between the lens and source samples (which determines the impact of intrinsic alignment), and calibration systematics.

4.2. Like-for-like Simulated Samples

Following I. G. McCarthy et al. (2025), we calculate simulated GGL profiles from the FLAMINGO lightcone maps. The observer's lightcone is approximated as concentric shells in comoving distance; see Appendix A of J. Schaye et al. (2023). At the redshifts of the kSZ and X-ray observations ($z \lesssim 1$), the shells are separated by $\Delta z = 0.05$. For each shell, the quantities of interest (e.g., dark matter mass, hot gas mass, kSZ) are represented by `HEALPix` maps (K. M. Górski et al. 2005). At a given redshift, z_0, we calculate the $\Delta\Sigma$ profile for each source in the simulated galaxy sample using the total mass map (gas, dark matter, stars, black holes, and neutrinos) closest in redshift to z_0. Per-pixel total masses are converted to comoving surface densities based on the pixel's comoving surface area. For computational efficiency, we use a high-resolution map ($N_{\rm side} = 16384$) when calculating the $\Delta\Sigma$ profile on small scales (<2 Mpc h^{-1}) and a lower-resolution ($N_{\rm side} = 2048$) map on larger scales. The individual $\Delta\Sigma$ profiles are then stacked in comoving radial bins between 0.2 and 75 Mpc h^{-1}.

For a given selection of simulated galaxies, we calculate the stacked $\Delta\Sigma$ profile for all lightcone shells between the minimum, $z_{\rm min}$, and maximum redshift, $z_{\rm max}$, of the observed sample. The final $\Delta\Sigma$ profile is then obtained by marginalizing over the observed sample's redshift distribution $n(z)$, approximated as a weighted sum from

$$\Delta\Sigma(R) = \int_{z_{\rm min}}^{z_{\rm max}} dz \Delta\Sigma_z(R) n(z). \quad (13)$$

This redshift marginalization was not included by I. G. McCarthy et al. (2025); however, it has a minimal impact on the inferred halo mass for the samples we consider.

4.2.1. SDSS and DESI kSZ Effect Profiles

For the kSZ effect profiles, replicating the SDSS and DESI selection functions would require careful treatment of the simulated stellar populations, including radiation transfer, dust reddening, and nucleosynthesis. Alternatively, the mean halo masses of the samples could be inferred from the galaxies' stellar masses (e.g., abundance matching). However, systematic uncertainties in stellar population synthesis modeling impart a significant uncertainty in the implied mean halo mass. In Figure 2, we compare the stellar mass distributions for the DESI samples from three publicly available stellar population synthesis catalogs: (i) DESI Legacy Imaging derived masses using a random forest algorithm (R. Zhou et al. 2023a),[9] (ii) `FastSpecFit` modeling of the DESI spectra (J. Moustakas et al. 2023),[10] and (iii) `CIGALE` modeling of the DESI spectra (M. Siudek et al. 2024).[11] Assuming the stellar-to-halo mass relation of the fiducial FLAMINGO simulation, the different stellar mass estimates correspond to $\gtrsim$0.1 dex variation in the mean halo mass.

Instead of relying on the stellar mass measurements, we select a sample of simulated galaxies that reproduces the observed GGL profile for each kSZ stack. I. G. McCarthy et al. (2025) demonstrated that selecting all simulated galaxies above a minimum stellar mass cut successfully reproduces the observed GGL profiles of the SDSS LOWZ and CMASS samples; this selection includes both centrals and satellites. In the simulations, galaxy stellar mass is defined as the total bound stellar mass within a radius of 50 kpc (physical units), centered on the particle with the minimum gravitational potential. For each observed sample, we fit for the minimum stellar mass cut that best fits the observed GGL profile by χ^2 minimization; as described above, the simulated $\Delta\Sigma$ profile is marginalized over the redshift distribution of the observed sample.

[9] https://data.desi.lbl.gov/public/ets/vac/stellar_mass/v1/
[10] https://data.desi.lbl.gov/doc/releases/dr1/vac/fastspecfit/
[11] https://data.desi.lbl.gov/doc/releases/edr/vac/cigale/

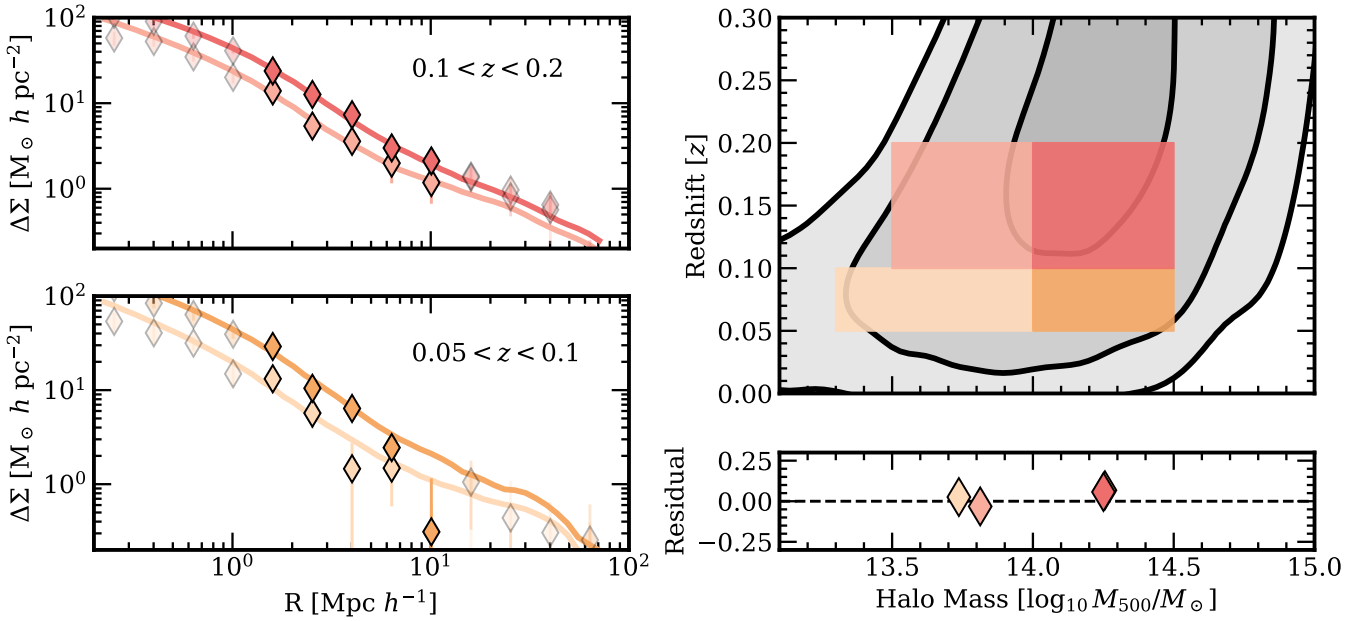

Figure 3. GGL halo mass inference for the eROSITA clusters. Left panels: measured GGL profiles for $0.05 < z < 0.1$ (bottom) and $0.1 < z < 0.2$ (top). For each redshift range, we consider two mass bins, defined in terms of the reported eRASS1 halo masses. The transparent points are omitted from the GGL fits (Section 4.2.2). The best-fitting FLAMINGO $\Delta\Sigma$ profiles are presented alongside the observations; for clarity, we only show the fiducial feedback strength simulation. Right panels: the redshift–halo mass distribution of eRASS1 (gray); contours correspond to the 39th, 86th, and 97th percentiles. The definitions of our GGL bins are demarcated by shaded regions. The bottom panel presents the residuals between the GGL derived mean halo masses and the eRASS1 catalog. The halo mass uncertainties are approximately 0.1 and 0.05 dex for the low and high mass bins, respectively (Table 3); the error bars are smaller than the markers.

While a stellar mass selection is unlikely to reproduce all properties of the SDSS and DESI samples, we adopt this selection function for our fiducial analysis because of its simplicity and its ability to reproduce the GGL measurements. In Appendix B, we demonstrate that our results are robust to large variations in the method of selecting simulated galaxies, such as selecting only centrals or drawing galaxies from a log–normal distribution on mass. I. G. McCarthy et al. (2025) also showed that the feedback constraints are consistent if galaxies are selected by cuts in both stellar mass and specific star formation rate. The robustness of our results to large variations in the selection function is expected, because the kSZ measurement is most sensitive to the mean halo mass of the sample.

For each DESI kSZ stack, we present the best-fit FLAMINGO GGL signals alongside the measurements in Figure 2, finding good agreement. The GGL fitting process is performed independently for the different FLAMINGO simulations; the inferred halo masses are nearly identical between the simulations (Tables 1 and 2). Based on the sizes of the Jackknife regions, we restrict the fits to < 9 and 20 comoving Mpc h^{-1} for the BGS and LRG samples, respectively.

4.2.2. eROSITA X-Ray Gas Masses

The eROSITA eRASS1 catalog provides halo mass measurements based on weak-lensing calibrated scaling relations between count rate and shear (V. Ghirardini et al. 2024). To validate the halo masses, we measure the GGL profile for four bins of eROSITA clusters (see Table 3). The GGL measurements for each X-ray sample are presented in Figure 3 and are described further in Appendix A.

The GGL signals are measured with the DES Y3 shear catalog because of its significantly larger overlap with the eRASS1 footprint (Figure 7). To mitigate cluster member contamination—cluster members can erroneously be included in the background source galaxy sample due to photometric redshift uncertainties (H. Hoekstra et al. 2012; D. Gruen et al. 2014; J. P. Dietrich et al. 2019; T. N. Varga et al. 2019)—we also consider the bespoke "blue" shear catalog of J. McCullough et al. (2024); blue shear omits red galaxies, which are more likely to be misidentified cluster members (see Appendix B.2). Our analysis of the cluster GGL measurements is restricted to 2–14 comoving Mpc h^{-1}; the omission of small scales is designed to suppress cluster member contamination, and the cut on large scales is dictated by the size of the Jackknife regions (Appendix B.2).

For each sample of clusters, we identify a selection of simulated FLAMINGO halos that best fits the observed GGL profile. Our fiducial selection function is a minimum halo mass cut; the derived halo masses are consistent if simulated clusters are instead drawn from a log–normal distribution in halo mass (Appendix B). The best-fit simulated GGL profiles are presented in Figure 3, alongside the measured profiles. For all four samples, the inferred mean halo mass is within 0.1 dex of the publicly reported mass.

5. Results: New kSZ and X-Ray Data Compared to FLAMINGO

We perform like-with-like comparisons between observational probes of the gas distribution (kSZ effect profiles and X-ray hot gas fractions) and the FLAMINGO simulations in Sections 5.1 and 5.2, respectively.

5.1. kSZ Effect Profiles

To perform a like-with-like comparison, we select a sample of simulated galaxies that reproduces the observed GGL signal for each kSZ measurement (Section 4.2.1). We measure the corresponding kSZ effect profiles from the simulations

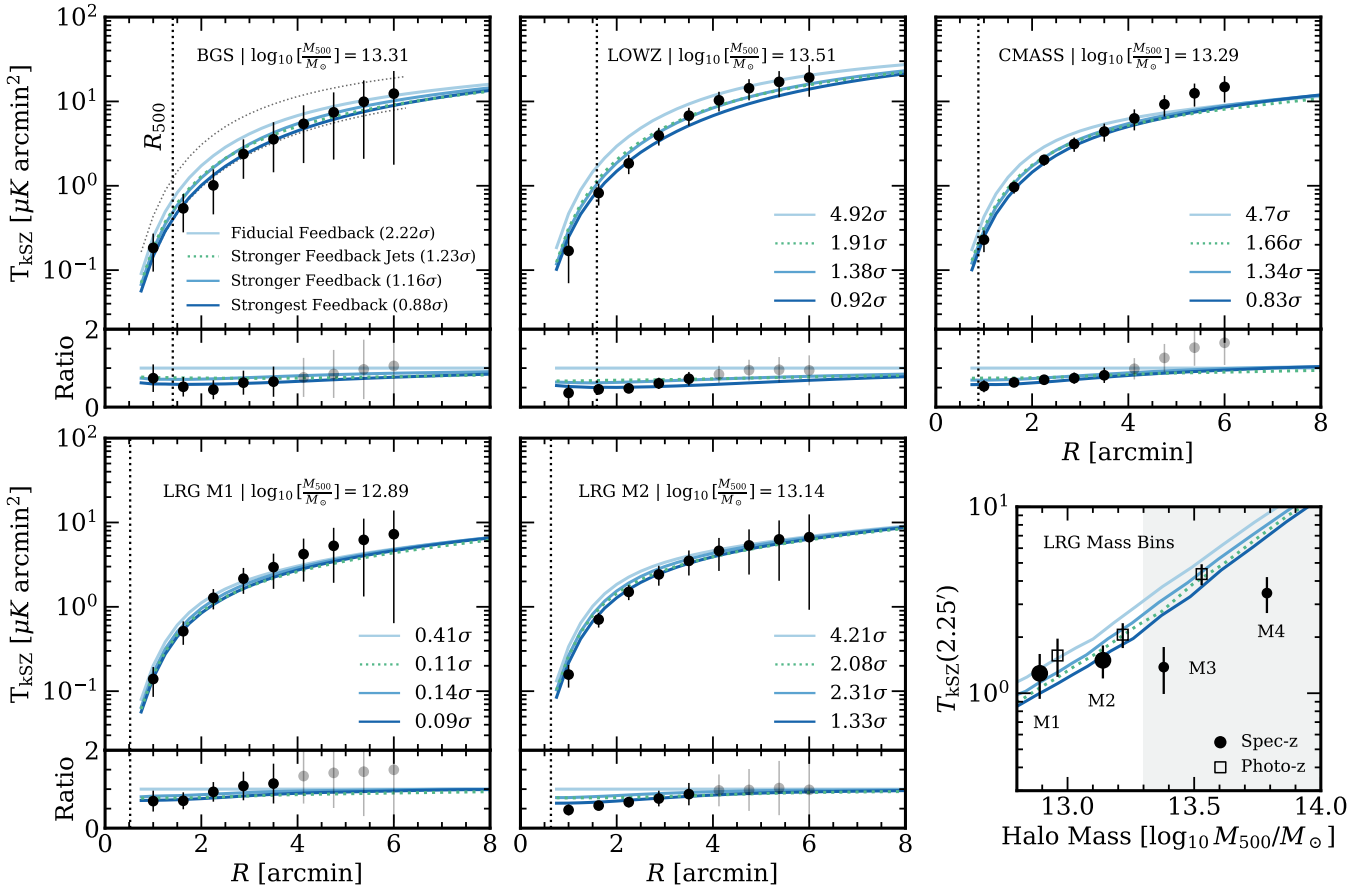

Figure 4. The kSZ measurements (black) compared with the GGL-selected predictions from the four FLAMINGO simulations we consider. We report the number of standard deviations by which each simulation prediction deviates from the observations. The kSZ effect measurement is highly correlated at larger angular separations, so these bins carry lower statistical weight. The bottom panels show the ratio of the data and the simulations to the fiducial feedback strength simulation. The vertical dotted line demarcates R_{500}. The bottom-right panel presents the amplitude of the stacked kSZ effect at $\theta = 2.25'$ for the spectroscopic (B. Ried Guachalla et al. 2025) and photometric (B. Hadzhiyska et al. 2025b) LRG kSZ mass bins ($z = 0.75$) as a function of GGL inferred halo mass, alongside the simulation predictions. All measurements require more feedback than fiducial FLAMINGO; however, the spectroscopic and photometric measurements require different feedback strengths at $M_{500} \gtrsim 2 \times 10^{13}\, M_\odot$ (shaded region) and are omitted from the primary analysis (see Appendix C).

following I. G. McCarthy et al. (2025). At a given redshift, we derive a `HEALPix` map of the kSZ effect from the Doppler B parameter (b) lightcone: $\Delta T_{\rm kSZ} = -bT_{\rm CMB}$. To mirror the observations, the kSZ effect maps are convolved with a Gaussian beam: FWHM of $1.'3$ and $1.'6$ for the SDSS and DESI kSZ stacks, respectively. We then stack the kSZ effect signal for the selected simulated galaxies using the CAP filter (Equation (4)). Analogous to the simulated $\Delta\Sigma$ profiles, we marginalize over the redshift distribution of the observed galaxy sample.

The simulated kSZ effect profiles are presented alongside the observations in Figure 4; the vertical lines correspond to R_{500}. For our fiducial analysis, we consider two SDSS kSZ stacks (LOWZ and CMASS) and three DESI kSZ stacks (BGS and two LRG mass bins: M1 and M2). The kSZ profiles of the fiducial simulation lie significantly above all five measurements. Since the kSZ effect is proportional to the gas mass, this offset shows that the simulated halos are more gas rich than is favored by the observations.

In the stronger feedback simulations, the AGNs more efficiently expel gas beyond the virial radius. The increased feedback depletes the halos' gas content and lowers the amplitude of the kSZ effect profile. At lower redshifts ($z < 0.6$: BGS, LOWZ, and CMASS), the strongest feedback simulation ($f_{\rm gas}\ -\ 8\sigma$) closely matches the observations, consistent with I. G. McCarthy et al. (2025). At $z = 0.75$, the two lower-mass LRG bins (M1 and M2) are also well described by the $f_{\rm gas}\ -\ 8\sigma$ FLAMINGO simulation. Combining all five kSZ measurements, the fiducial FLAMINGO simulation is $>8\sigma$ from the data. The stronger feedback simulations ($f_{\rm gas}\ -\ 4\sigma$ and Jet_$f_{\rm gas}\ -\ 4\sigma$) provide a better fit but still deviate by approximately 3.5σ. The strongest feedback simulation reproduces the measurements best (2σ from the data). The goodness-of-fits are calculated using the full covariance matrices of the measurements to account for the strong correlations in the outermost bins.

We exclude the highest-mass spectroscopic LRG bins (M3 and M4) from our fiducial analysis. At these masses ($M_{500} > 2 \times 10^{13}\ M_\odot$), the measurements of B. Ried Guachalla et al. (2025), which use spectroscopic redshifts, and the measurements of B. Hadzhiyska et al. (2025b), which use photometric redshifts, imply different feedback strengths; at lower masses, the two methods agree well. The two highest-mass LRG bins (M3 and M4) from the spectroscopic measurements require more gas expulsion ($>4\sigma$ from the data) than the strongest feedback FLAMINGO simulation ($f_{\rm gas}\ -\ 8\sigma$), but the photometric measurements are well matched by $f_{\rm gas}\ -\ 8\sigma$ (at the 2σ level). The spectroscopic and photometric measurements both imply stronger feedback than the fiducial FLAMINGO simulation.

We present a full analysis of the photometric measurements and high-mass spectroscopic bins in Appendix C. Differences between the spectroscopic and photometric kSZ measurements could stem from sample selection, e.g., overdense regions may be undersampled in the spectroscopic sample due to fiber collisions. However, we find that the stellar-to-halo-mass relations inferred from the photometric and spectroscopic samples are consistent, and we have demonstrated that our conclusions are robust to assuming the galaxy samples are composed of only centrals or centrals and satellites. The discrepancy may also arise from uncertainties in the photometric redshifts. Further study of observational uncertainties and potential systematics in the simulation comparison is warranted.

From our like-with-like comparisons, all observed kSZ effect profiles are discrepant with the fiducial FLAMINGO simulation; the fiducial simulation overpredicts the amplitude of the kSZ signal, showing the halos are too gas rich. Of the FLAMINGO simulations, the observations are best fit by the strongest feedback variant ($f_{\rm gas}$ $-$ 8σ).

5.2. X-Ray Gas Fractions

The $f_{\rm gas}$–M_{500} trend is indicative of the strength of feedback and has been used to calibrate cosmological hydrodynamical simulations (e.g., R. Kugel et al. 2023). The eROSITA survey has identified thousands of X-ray groups and clusters between $0.0 \lesssim z \lesssim 1.3$ and $10^{12} \lesssim M_{500}/M_{\odot} \lesssim 10^{15}$. The lower-mass halos ($\lesssim 10^{14}$ $M_{\odot}$) are particularly informative for studying feedback because the ICM is most depleted in these shallower potential wells. However, detecting and characterizing low-mass clusters is observationally challenging. These clusters are naturally fainter and less rich, which limits their detection to lower redshifts and increases the contamination fraction. In Section 4.2.2, we validated the eROSITA halo mass estimates with GGL (Figure 3).

Figure 5 compares the halo masses and gas fractions of our four cluster samples with the FLAMINGO simulations. We adopt the GGL derived halo masses and the eROSITA reported gas mass measurements. The eROSITA gas mass measurements assume R_{500} corresponding to the eROSITA halo mass estimates, which differ (marginally) from our GGL measurements; the difference in enclosed gas fraction is expected to be small (M. Velliscig et al. 2014; R. Kugel et al. 2023), especially with our GGL halo masses within <0.1 dex of the publicly reported eROSITA masses. The eROSITA gas fractions agree remarkably well with the strongest feedback FLAMINGO simulation. To reconcile our eROSITA samples with the fiducial simulation, the stacked halo masses would need to be 0.4 dex lower. However, the statistical and systematic uncertainties on our M_{500} measurements are below 0.15 dex. We discuss potential systematics in the X-ray observations in Section 6.1.

6. Discussion

We find a consistent picture of strong baryon feedback across halo mass ($10^{13} < M_{500}/M_{\odot} < 10^{14}$) and redshift ($z < 1$); see Figure 6. Our joint analysis of kSZ, X-ray, and GGL measurements reveals that the fiducial FLAMINGO simulation does not expel enough gas beyond R_{500} from groups and clusters. This is particularly striking because the FLAMINGO matter power spectrum is more suppressed by

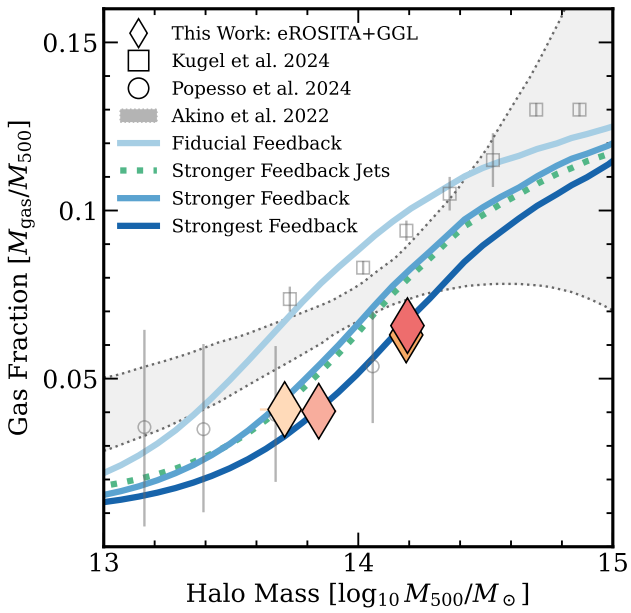

Figure 5. The hot gas fraction $f_{\rm gas}$ within R_{500} as a function of halo mass M_{500} in groups and clusters. Our independent halo masses for bins of eROSITA detected clusters are shown as diamonds, with the colors following Figure 3. We report halo mass uncertainties of < 0.1 dex (see Table 3); the error bars are smaller than the markers. The pre-eROSITA $f_{\rm gas}$–M_{500} relations of D. Akino et al. (2022) and R. Kugel et al. (2023) are included for reference, alongside the stacking measurements of P. Popesso et al. (2024b). We also present the mean $f_{\rm gas}$–M_{500} relation from the four FLAMINGO simulations we consider.

baryons than other widely used simulations, such as MillenniumTNG (R. Pakmor et al. 2023), EAGLE (J. Schaye et al. 2015), and FABLE (N. A. Henden et al. 2018). For every observation, strong feedback provides a better fit to the data than the fiducial FLAMINGO simulation.

At $z < 0.6$, all of the observations are remarkably consistent with the strongest feedback simulation ($f_{\rm gas}$ $-$ 8σ). The simulation simultaneously reproduces the eROSITA+GGL X-ray gas fractions ($z \sim 0.1$) and the kSZ effect profiles of SDSS LOWZ and CMASS and DESI BGS. At higher redshifts ($z = 0.75$), the lower-mass (M1 and M2) LRG kSZ effect profiles are also consistent with $f_{\rm gas}$ $-$ 8σ. The highest-mass LRG bins (M3 and M4) potentially require even stronger feedback, but we caution that the kSZ profiles from the spectroscopic (B. Ried Guachalla et al. 2025) and photometric (B. Hadzhiyska et al. 2025b) based measurements imply different feedback strengths at these masses; see Appendix C.

6.1. On the Consistency of X-Ray Observations

The X-ray gas fractions of groups and clusters are a long standing probe of baryon feedback. eROSITA observations now indicate that groups and clusters are, on average, more gas-depleted than previously found. In Figure 5, we present the mean gas fractions for bins of eROSITA detected clusters, using our GGL derived mean halo masses. The fiducial FLAMINGO simulation was calibrated to a collection of pre-eROSITA X-ray gas fractions (R. Kugel et al. 2023), including a selection of surveys without explicit selection effect corrections: A. Vikhlinin et al. (2006), B. J. Maughan et al. (2008), J. Rasmussen & T. J. Ponman (2009), M. Sun et al. (2009), G. W. Pratt et al. (2010), Y.-T. Lin et al. (2012), T. F. Laganá et al. (2013), A. J. R. Sanderson et al. (2013), A. H. Gonzalez et al. (2013), L. Lovisari et al. (2015), H. Hoekstra et al. (2015), R. J. Pearson

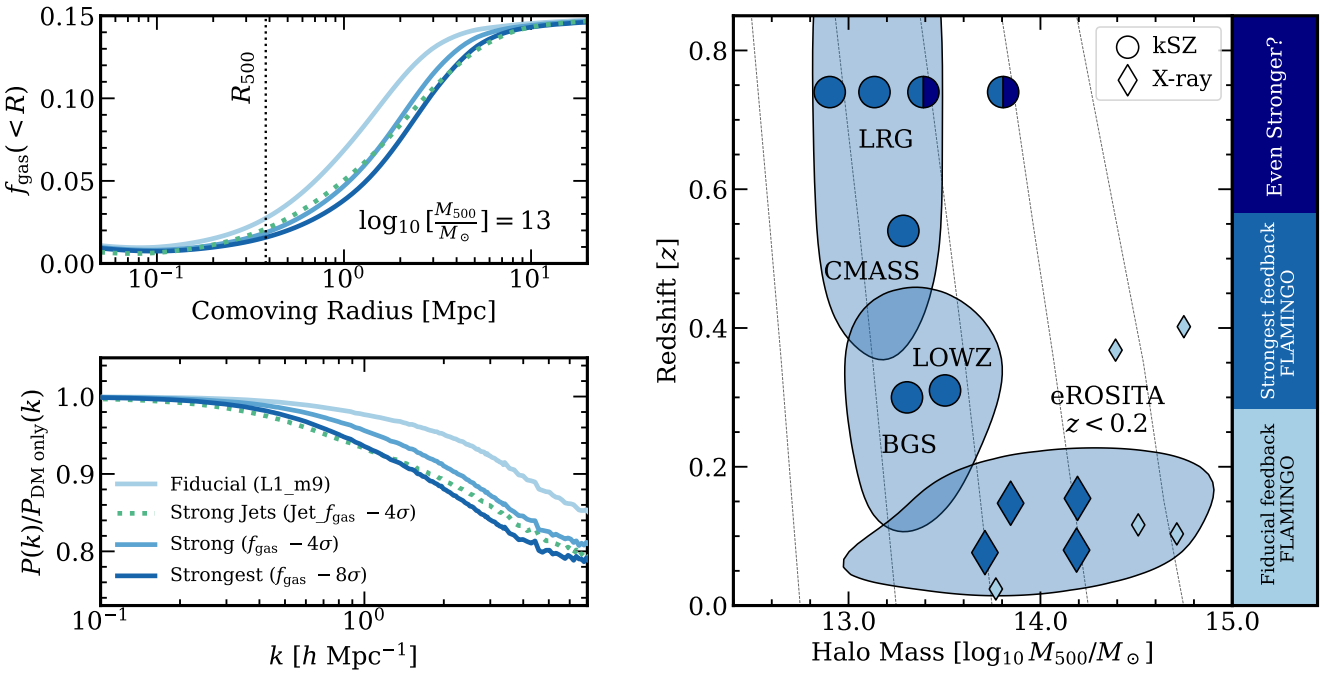

Figure 6. Across a wide range of redshift ($z < 1$) and halo mass ($\log_{10} M_{500}/M_\odot = 13 - 14$), the gas distribution is well described by the strongest feedback FLAMINGO simulation ($f_{\rm gas} - 8\sigma$). Left panels: demonstration of how the different FLAMINGO feedback prescriptions impact the gas distribution. For the four simulations we consider, the top panel presents the enclosed gas fraction profile of a $M_{500} = 10^{13}\,M_\odot$ halo, and the bottom panel shows the matter power spectrum relative to a dark-matter-only universe. Right panel: the average redshifts and halo masses of the kSZ stacks and our bins of eROSITA clusters, colored by the preference for fiducial (light blue), strongest (blue), or even stronger feedback (dark blue), in terms of the FLAMINGO suite. We include the distributions of the DESI BGS and LRG samples, as well as the eROSITA eRASS1 clusters ($z < 0.2$); contours correspond to the 86th percentile. The mean redshifts and halo masses for a selection of pre-eROSITA X-ray surveys are included in light blue, reflecting their apparent preference for the fiducial simulation (A. Vikhlinin et al. 2006; B. J. Maughan et al. 2008; A. H. Gonzalez et al. 2013; L. Lovisari et al. 2015; D. Eckert et al. 2016). The dotted lines show the mean growth histories of halos, binned by their redshift zero mass.

et al. (2017), S. L. Mulroy et al. (2019), and L. Lovisari et al. (2020); the mean gas fraction relation from these surveys is presented in Figure 5. R. Kugel et al. (2023) also considered the $f_{\rm gas}$–M_{500} relation of D. Akino et al. (2022), shown as a gray band in Figure 5. The D. Akino et al. (2022) model is derived from the HSC–XXL sample, with GGL measured halo masses and corrections for selection effects. Our GGL calibrated eROSITA bins lie significantly below the R. Kugel et al. (2023) relation and also fall below the D. Akino et al. (2022) model.

Selection effects potentially contribute to the apparent discrepancy between the population of eROSITA clusters and the prior gas fraction measurements. Previous studies often selected X-ray bright nearby group size halos from the ROSAT All-Sky survey (J. Truemper 1982; W. Voges et al. 1999). Because X-ray luminosity is proportional to density and gas mass (along with a temperature dependence), X-ray selected samples are biased to concentrated gas-rich halos. Compared with previous samples, the lower mean gas mass fractions of the eROSITA catalog could reflect its greater completeness. The population of eROSITA detected groups and clusters is also shaped by selection effects; at $z < 0.2$, the completeness of the eRASS1 catalog falls significantly below $10^{14} M_\odot$ (R. Seppi et al. 2022; P. Popesso et al. 2024; I. Marini et al. 2024). In this paper, we therefore limit our X-ray detected eROSITA sample to low-redshift massive halos. Forward modeling the X-ray selection function for the eROSITA gas mass fraction measurements is a critical next step (e.g., R. Seppi et al. 2022; N. Clerc et al. 2024; I. Marini et al. 2024; R. Seppi et al. 2025). Studies that have fully accounted for the eROSITA selection function also require strong feedback. Y. E. Bahar et al. (2024) compared the entropy of eROSITA-selected galaxy groups, with consideration for the selection function, with several cosmological hydrodynamic simulations (MillenniumTNG, Magneticum, OWLS) and found they exhibit milder feedback than the observations require, consistent with our findings on the gas mass fractions.

Studies have also attempted to bypass the X-ray selection bias altogether. P. Popesso et al. (2024b) measured the stacked gas fractions of optically selected groups using eROSITA images. The groups were identified from the GAMA survey using the friends-of-friends algorithm (A. S. G. Robotham et al. 2011; S. P. Driver et al. 2022). While P. Popesso et al. (2024b) mitigates the effects of X-ray selection, optical group finders can be contaminated by >30% (R. Seppi et al. 2025) and the halo mass estimates rely on an optical scaling relation (I. Marini et al. 2025). The measured $f_{\rm gas}$–M_{500} relation from P. Popesso et al. (2024b) is presented in Figure 5, alongside our GGL calibrated bins. Despite the differences in selection, the results of P. Popesso et al. (2024b) are consistent with our GGL calibrated eROSITA gas fractions within 1σ.

Halo mass estimation is another source of systematic bias for X-ray gas mass fractions. Prior studies often derived total halo masses assuming hydrostatic equilibrium. Contributions from nonthermal pressure can bias hydrostatic masses low by approximately 30% (H. Hoekstra et al. 2015; D. Eckert et al. 2016; R. Kugel et al. 2023; M. Muñoz-Echeverría et al. 2024); this bias is dependent on cluster mass (J. Braspenning et al. 2025). The eRASS1 halo masses are estimated from a weak-lensing calibrated scaling relation (V. Ghirardini et al. 2024). While the scaling relation is limited by the calibration data, our

GGL validates the eROSITA reported masses in the previously uncertain low-mass regime.

X-ray flux calibration and the assumed ICM metallicity are potential additional sources of minor bias. For instance, E. Bulbul et al. (2024) found that the eROSITA derived luminosities are approximately 15% lower than previously inferred with Chandra for a sample of South Pole Telescope (SPT)-selected galaxy clusters; this offset corresponds to gas mass estimates skewed lower by roughly 7% (at fixed temperature, X-ray luminosity is proportional to gas density squared); our results are insensitive to this offset, but further study is warranted. The impact of metallicity assumptions is also expected to be small, contributing less than a few percent to the uncertainty (A. Liu et al. 2022).

Forward modeling of X-ray and optical selection effects will be critical in reducing systematic uncertainties in the $f_{\rm gas} - M_{500}$ relation. However, a consensus picture of strong feedback is already emerging. Optical (P. Popesso et al. 2024b) and X-ray (E. Bulbul et al. 2024) selected samples are consistent at $10^{14}\,M_{\odot}$ and require more gas depletion than previously believed. A comprehensive study of gas mass fractions in eROSITA-selected galaxy groups, accounting for the relevant selection effects, is warranted to obtain a complete picture of feedback across a wider mass range (Ding et al. in prep).

6.2. Implications for Feedback Models

Our analysis of kSZ, X-ray, and GGL measurements reveals that more gas is expelled beyond R_{500} across redshift ($z < 1$) and mass ($10^{13} < M_{500}/M_{\odot} < 10^{14}$) than predicted by the fiducial FLAMINGO simulation, even though the gas fractions in the fiducial simulation are actually lower than other cosmological simulations, including MillenniumTNG (R. Pakmor et al. 2023), EAGLE (J. Schaye et al. 2015), and FABLE (N. A. Henden et al. 2018). Of the FLAMINGO simulations, the strongest feedback variant ($f_{\rm gas} - 8\sigma$) reproduces the kSZ and X-ray observations best. The landscape of observations that we consider is summarized in Figure 6: the eROSITA X-ray gas fractions and SDSS/DESI+ACT kSZ samples are shown as a function of redshift and halo mass, alongside a selection of pre-eROSITA X-ray data (A. Vikhlinin et al. 2006; B. J. Maughan et al. 2008; A. H. Gonzalez et al. 2013; L. Lovisari et al. 2015; D. Eckert et al. 2016). Our results present a consistent picture of strong baryon feedback and suggest that baryons impact the matter power spectrum more than predicted by recent simulations.

Evidence of strong feedback is mounting from a wide range of observables (A. Amon & G. Efstathiou 2022; A. Schneider et al. 2022; C. Preston et al. 2023; L. Bigwood et al. 2024; B. Hadzhiyska et al. 2025a; M. Kovač et al. 2025; A. La Posta et al. 2025; I. G. McCarthy et al. 2025; S. Pandey et al. 2025; R. Reischke & S. Hagstotz 2025; N. Dalal et al. 2026). By jointly modeling the CMASS kSZ effect profile and eROSITA X-ray gas mass fraction measurements with the baryonification framework, M. Kovač et al. (2025) constrained the suppression of the matter power spectrum and found excellent agreement with the $f_{\rm gas} - 8\sigma$ simulation. Using a sample of tSZ selected clusters from ACT DR6, N. Dalal et al. (2026) inferred similarly strong suppression of the matter power spectrum. Strong feedback has also been inferred from comparing hydrodynamical simulations to kSZ and X-ray observations (I. G. McCarthy et al. 2018; J. Schaye et al. 2023; B. Hadzhiyska et al. 2025b; I. G. McCarthy et al. 2025; B. Ried Guachalla et al. 2025). Using the GGL mean halo mass constraints presented here, L. Bigwood et al. (2025b) extended this work to benchmark a collection of recent hydrodynamical simulations (FLAMINGO, ANTILLES, BAHAMAS, SIMBA, FABLE, and their variants) against the DESI+ACT kSZ effect profiles, finding the strong feedback variants reproduce the data best.

Within the context of the FLAMINGO simulations, the strongest feedback model ($f_{\rm gas} - 8\sigma$) produces the best match to the kSZ effect and gas fraction measurements examined here, implying significant suppression of the matter power spectrum at $k > 1\,h\,{\rm Mpc}^{-1}$. However, it should be noted that J. Braspenning et al. (2024) found that this model deviates from the pre-eROSITA observed cluster scaling relations (L–T and L–M). Recently, D. Eckert et al. (2026) reported the same deviation when comparing the FLAMINGO simulations with the X-GAP sample. The more moderate feedback variants (e.g., $f_{\rm gas} - 4\sigma$) are still consistent with the cluster measurements but do not reproduce the kSZ measurements as well. It will be interesting to explore whether variations in the implemented feedback modeling can successfully reproduce these observations simultaneously and potentially make distinct predictions for other observables. For example, studies have indicated that the properties of clusters are also sensitive to the *mode* of AGN outbursts (e.g., radiative versus jet; see J. Braspenning et al. 2024; L. Bigwood et al. 2025a). E. Quataert & P. F. Hopkins (2025) recently proposed that cosmic-ray feedback could be substantial in massive halos, which could also alter the interpretation of X-ray spectra (P. F. Hopkins et al. 2026). As we explore variations in the modeling, we should also investigate possible remaining biases in the observations. This necessitates forward modeling the data from the simulations as faithfully as possible, including kSZ extraction from realistic synthetic CMB maps and applying the same velocity reconstruction methods as the observations, as well as selecting simulated groups and clusters with the same method used for the eROSITA X-ray data. This is the subject of ongoing work.

7. Conclusions

The efficiency and extent of gas expulsion beyond R_{500} and its impact on the large-scale matter distribution is unclear. To confront this uncertain landscape, a multiprobe view of the gas content of groups and clusters is required. The aim of this work is to jointly constrain the gas distribution with kSZ effect profiles, X-ray gas mass fractions, and GGL. We benchmark the measurements against the suite of 1 Gpc^3 FLAMINGO simulations (J. Schaye et al. 2023). The main results of this study are as follows:

1. Our GGL provides precise mean halo mass constraints for the eROSITA X-ray gas mass measurements (E. Bulbul et al. 2024) and the SDSS/DESI+ACT kSZ effect profiles (E. Schaan et al. 2021; B. Ried Guachalla et al. 2025). The X-ray and kSZ measurements together span a wide range of halo masses ($M_{500} = 10^{13-14} M_{\odot}$), redshifts ($0 < z < 1$), and radial scales ($<$2–3 R_{500}). By jointly analyzing the kSZ and X-ray measurements with GGL, we address the leading uncertainties in constraining the gas distribution: (i) the strength of feedback inferred from the measurements is degenerate with halo

mass and satellite fraction and (ii) kSZ and X-ray measurements on their own span limited ranges of halo mass and redshift. We select simulated galaxy samples that reproduce the measured GGL signal to ensure that the halo mass and satellite fraction of the simulated and observed samples match. We demonstrate that this calibration is insensitive to the assumed feedback strength in the simulation, as well as changes in the lensing (e.g., choice of imaging survey and selection of background sources); see Appendix B.

2. The fiducial FLAMINGO simulation is significantly disfavored by the kSZ effect profiles ($>8\sigma$ combined) and the new eROSITA X-ray gas fractions. For groups and low-mass clusters, FLAMINGO halos are too gas rich within R_{500}. The fiducial simulation was calibrated on the pre-eROSITA gas fractions of low-redshift galaxy groups and clusters (R. Kugel et al. 2023), which were potentially biased toward gas-rich halos.
3. The simulation with the strongest baryon feedback (FLAMINGO $f_{\rm gas}-8\sigma$) provides a good match to the SDSS/DESI+ACT kSZ and eROSITA X-ray measurements. This simulation was calibrated to pre-eROSITA gas fractions systematically shifted down, and the strong feedback is achieved by more powerful but less-frequent AGN outbursts. The success of the strongest feedback simulation in describing the gas distribution to several R_{500} across group and cluster masses and between $0 < z < 1$ forms strong indirect evidence for extreme suppression of the matter power spectrum ($\sim$10% at $k = 1\,h\,{\rm Mpc}^{-1}$). This conclusion on where the gas is distributed is independent of the particular feedback mechanism implemented in FLAMINGO.

Outlook: Further exploration of feedback implementations is warranted. The strongest feedback FLAMINGO simulation ($f_{\rm gas}-8\sigma$) provides an excellent description of where the gas is distributed, but it deviates from observed cluster scaling relations (J. Braspenning et al. 2024; D. Eckert et al. 2026). While the moderate feedback FLAMINGO variants (e.g., $f_{\rm gas}-4\sigma$) are more consistent with the cluster scaling relations, they are less compatible with the kSZ measurements. Combining the five kSZ measurements included in our fiducial analysis, the strongest feedback simulation is 2σ from the data, while the more moderate simulations ($f_{\rm gas}-4\sigma$ and Jet_$f_{\rm gas}-4\sigma$) are 3.5σ from the data. Since the properties of clusters are also sensitive to the mode of AGN feedback (e.g., radiative versus jet; see J. Braspenning et al. 2024; L. Bigwood et al. 2025a), it will be informative to explore whether variations in the subgrid AGN feedback modeling or other mechanisms of gas expulsion (e.g., cosmic-ray transport; E. Quataert & P. F. Hopkins 2025) can more successfully reproduce all observations simultaneously.

In this work, we used GGL to resolve uncertainties in interpreting the kSZ measurements related to the mean halo mass and satellite fraction; however, there are still remaining biases to be explored. In particular, our analysis omitted the two high-mass DESI LRG kSZ bins (M3 and M4), because the kSZ stacks measured from spectroscopic and photometric redshifts imply different feedback strengths at these masses (Appendix C). The photometric measurements (B. Hadzhiyska et al. 2025b) are consistent with the strongest feedback FLAMINGO variant ($f_{\rm gas}-8\sigma$), while the spectroscopic measurements (B. Ried Guachalla et al. 2025) appear to require even stronger gas expulsion ($>4\sigma$ discrepant from the strongest feedback simulation). Both the photometric and spectroscopic kSZ measurements require stronger feedback than the fiducial FLAMINGO simulation, which was calibrated to reproduce pre-eROSITA data. This warrants further investigation into the measurements, including differences in sample selection and potential systematics in the velocity reconstruction. To more fully account for systematics in future like-with-like simulation comparisons, the simulated peculiar velocities should be reconstructed using the same method as the observations; in this work, we use the true peculiar velocities from FLAMINGO and accounted for inaccuracies in the observed velocities using the correction factors of E. Schaan et al. (2021) and B. Hadzhiyska et al. (2024).

Forward modeling of the X-ray gas fractions is also a necessary step. X-ray detected samples are incomplete at lower masses ($\lesssim 10^{14}\,M_{\odot}$) and potentially biased toward gas-rich halos (R. Seppi et al. 2022; I. Marini et al. 2024). In this work, we did not apply an X-ray selection function to the simulated halos and instead limited our comparison to massive halos ($\gtrsim 10^{14}\,M_{\odot}$) from the eROSITA sample, which is more complete than prior X-ray selected surveys. We demonstrated that our sample of eROSITA detected clusters is consistent with the gas fractions of optically selected halos (P. Popesso et al. 2024b). Forward modeling the emission from simulated halos is also informative for investigating systematics in the measurement of gas mass from X-ray images.

Accurately constraining the suppression of the matter power spectrum due to baryon feedback is vital to extracting cosmological information from the nonlinear regime. From a consistent analysis of kSZ, X-ray, and GGL measurements, we report a consensus picture of strong gas expulsion: across group and cluster masses and between $0 < z < 1$, the gas distribution is well described by the strongest feedback FLAMINGO simulation ($f_{\rm gas}-8\sigma$) out to several R_{500}. Independent of the mechanism that redistributes gas on such large radial scales, the agreement between the strongest feedback simulation and the data forms a compelling picture of significant suppression of the matter power spectrum: $\sim$10% at $k = 1\,h\,{\rm Mpc}^{-1}$. This level of suppression is stronger than most state-of-the-art hydrodynamical simulations and has implications for current weak-lensing studies and next-generation lensing surveys (e.g., Vera Rubin, Euclid, and Roman; R. Akeson et al. 2019; Ž. Ivezić et al. 2019; Euclid Collaboration et al. 2025). Future survey data from Simons Observatory and NewAthena will provide the next decisive tests on baryon feedback (e.g., K. Nandra et al. 2013).

Acknowledgments

We thank Bernardita Ried Guachalla and Boryana Hadzhiyska for helpful feedback and making the data available to us. We also thank Sven Heydenreich for helpful guidance in using DESI data and George Efstathiou and Simone Ferraro for useful feedback on this manuscript. J.S. acknowledges support by the National Science Foundation Graduate Research Fellowship Program under grant DGE-2039656. E.B. acknowledges financial support from the European Research Council (ERC) Consolidator Grant under the European Union's Horizon 2020 research and innovation program (grant agreement CoG DarkQuest No. 101002585). Any opinions, findings, and conclusions or recommendations expressed in this material are those of the author(s) and do not necessarily reflect the views of the National

Science Foundation. This work was supported by the Science and Technology Facilities Council (grant No. ST/Y002733/1). This work used the DiRAC@Durham facility managed by the Institute for Computational Cosmology on behalf of the Science and Technology Facilities Council (STFC) Distributed Research Utilizing Advanced Computing (DiRAC) High Performance Computing Facility (www.dirac.ac.uk). The equipment was funded by BEIS capital funding via STFC capital grants ST/K00042X/1, ST/P002293/1, ST/R002371/1, and ST/S002502/1, Durham University and STFC operations grant ST/R000832/1. DiRAC is part of the National e-Infrastructure.

The authors are honored to be permitted to conduct scientific research on I'oligam Du'ag (Kitt Peak), a mountain with particular significance to the Tohono O'odham Nation.

KiDS 1000. Based on observations made with ESO Telescopes at the La Silla Paranal Observatory under program IDs 177.A-3016, 177.A-3017, 177.A-3018, and 179.A-2004, and on data products produced by the KiDS consortium. The KiDS production team acknowledges support from: Deutsche Forschungsgemeinschaft, ERC, NOVA, and NWO-M grants; Target; the University of Padova, and the University Federico II (Naples).

DES Y3. This project used public archival data from the Dark Energy Survey (DES). Funding for the DES Projects has been provided by the U.S. Department of Energy, the U.S. National Science Foundation, the Ministry of Science and Education of Spain, the Science and Technology Facilities-Council of the United Kingdom, the Higher Education Funding Council for England, the National Center for Supercomputing Applications at the University of Illinois at Urbana-Champaign, the Kavli Institute of Cosmological Physics at the University of Chicago, the Center for Cosmology and Astro-Particle Physics at the Ohio State University, the Mitchell Institute for Fundamental Physics and Astronomy at Texas A&M University, Financiadora de Estudos e Projetos, Fundação Carlos Chagas Filho de Amparo à Pesquisa do Estado do Rio de Janeiro, Conselho Nacional de Desenvolvimento Científico e Tecnológico and the Ministério da Ciência, Tecnologia e Inovação, the Deutsche Forschungs-gemeinschaft, and the Collaborating Institutions in the Dark Energy Survey. The Collaborating Institutions are Argonne National Laboratory, the University of California at Santa Cruz, the University of Cambridge, Centro de Investigaciones Energéticas, Medioambientales y Tecnológicas-Madrid, the University of Chicago, University College London, the DES-Brazil Consortium, the University of Edinburgh, the Eidgen-össische Technische Hochschule (ETH) Zürich, Fermi National Accelerator Laboratory, the University of Illinois at Urbana-Champaign, the Institut de Ciències de l'Espai (IEEC/CSIC), the Institut de Física d'Altes Energies, Lawrence Berkeley National Laboratory, the Ludwig-Maximilians Universität München and the associated Excellence Cluster Universe, the University of Michigan, the National Optical Astronomy Observatory, the University of Nottingham, The Ohio State University, the OzDES Membership Consortium, the University of Pennsylvania, the University of Portsmouth, SLAC National Accelerator Laboratory, Stanford University, the University of Sussex, and Texas A&M University. Based in part on observations at Cerro Tololo Inter-American Observatory, National Optical Astronomy Observatory, which is operated by the Association of Universities for Research in Astronomy (AURA) under a cooperative agreement with the National Science Foundation.

Appendix A
Galaxy–Galaxy Lensing

In this paper, we measure stacked GGL profiles using three shear catalogs: DES Y3, HSC Y3, and KiDS 1000. The on-sky footprints and tomographic redshift distributions of the lensing surveys are presented in Figure 7, alongside DESI DR1 and eRASS1. The lensing catalogs are described in Appendix A.1. We describe corrections to the GGL estimator in Appendix A.2.

We closely follow the methodology described in J. U. Lange et al. (2024) and S. Heydenreich et al. (2025) for our DESI GGL measurements. For the BGS lenses, we combine the GGL measurements across DES Y3, HSC Y3, and KiDS 1000 by an inverse-variance weighted average. The calibrated measurements from the individual surveys are statistically consistent within 2σ (Figure 8). For the LRG lenses, only HSC has sufficiently high-redshift tomographic bins to measure the GGL signal over the full redshift range $z = 0.4$–1.1. To gauge whether the lensing surveys are consistent, we measure the GGL signal for low-redshift LRG lenses ($z = 0.4$–0.5) with DES, HSC, and KiDS; we again find that the measurements are statistically consistent within 2σ (Figure 8). For our analysis of the LRG lenses, we adopt the HSC GGL measurement using the full redshift range $z = 0.4$–1.1. The consistency between the lensing surveys was previously established by S. Heydenreich et al. (2025; also see A. Amon et al. 2023), which found that the GGL signals from the same data we consider are consistent after correcting the mean redshifts of the HSC tomographic bins; we include the HSC correction following X. Li et al. (2023) and S. Heydenreich et al. (2025).

For the eROSITA lenses, we rely on the DES Y3 shear catalog, because of its significant overlap with the eROSITA footprint (Figure 7).

A.1. Weak-lensing Catalogs

The Dark Energy Survey (DES) imaged over 5000 deg^2 of the Southern sky (*grizY*) with the Blanco 4 m telescope at Cerro Telolo Inter-American Observatory (The Dark Energy Survey Collaboration 2005). We use the DES Y3 shear catalog,[12] which consists of >100 million galaxies to $i < 23.5$ mag (M. Gatti et al. 2021; I. Sevilla-Noarbe et al. 2021). DES Y3 ellipticities are measured via METACALIBRATION, in which the shape measurement biases are inferred by artificially shearing the observed images (E. Huff & R. Mandelbaum 2017; E. S. Sheldon & E. M. Huff 2017; M. Gatti et al. 2021). The tomographic redshift distributions are calibrated following J. Myles et al. (2021), and the shear calibration is from N. MacCrann et al. (2022). We also consider the DES Y3 "blue shear" catalog of J. McCullough et al. (2024), which omits red source galaxies (Appendix B.2).

KiDS (J. T. A. de Jong et al. 2013) was carried out at Paranal from 2011–2019 using OmegaCAM on the VLT Survey Telescope. We consider the fourth data release (DR4[13]; K. Kuijken et al. 2019), which covers approximately 1000 deg^2. Shapes are measured with the *lensfit* algorithm

[12] https://des.ncsa.illinois.edu/releases/y3a2
[13] https://kids.strw.leidenuniv.nl/DR4/index.php

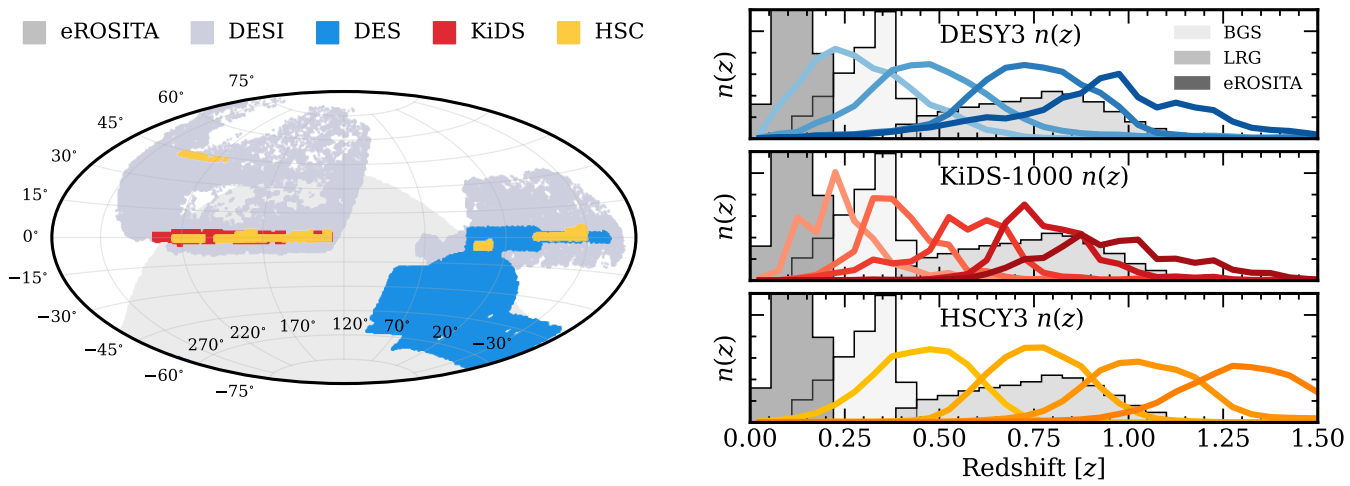

Figure 7. Left panel: the footprint of the DESI DR1 data (the BGS and LRG samples are shown in light blue), eRASS1 (gray), and the three imaging surveys: DES (blue), KiDS (red), and HSC (yellow). Right panels: the redshift distributions $n(z)$ of the lenses for our galaxy–galaxy lensing: eROSITA eRASS1 groups and clusters and DESI DR1 BGS and LRG. Each row presents the $n(z)$ of a different lensing survey's tomographic bins: DES Y3, KiDS 1000, and HSC Y3. For measuring the GGL signal, we only consider source tomographic bins sufficiently behind the lens ($\bar{z}_{\mathrm{bin}\,i} > z_l + 0.1$, where $\bar{z}_{\mathrm{bin}\,i}$ is the average redshift of the ith tomographic bin, and z_l is the lens redshift).

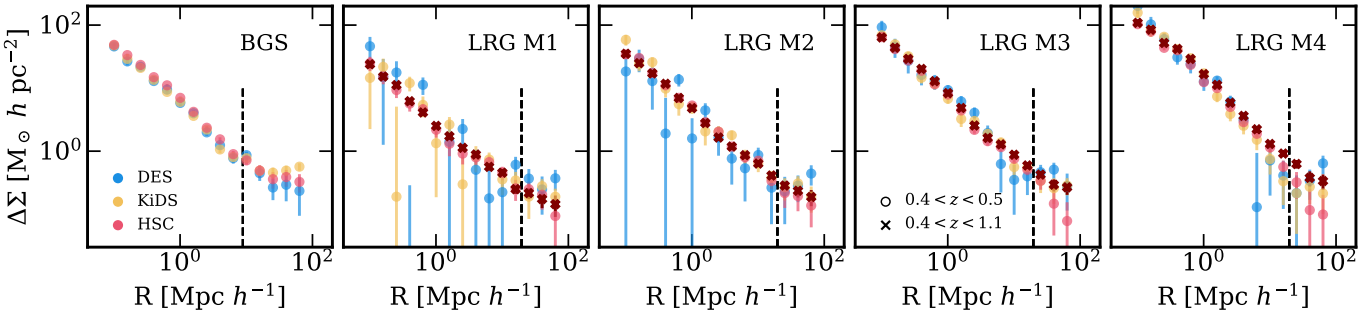

Figure 8. The excess surface density measurements for the DESI lenses using the different lensing surveys. Each column presents a different lens sample. For the LRG samples, only HSC has a tomographic bin at sufficiently high redshift to measure the GGL signal for the full redshift range ($z = 0.4$–1.1); we therefore present the GGL measurement for a selection of low-redshift lenses ($z = 0.4$–0.5) for DES, KiDS, and HSC, alongside the full redshift range measurement from HSC. The vertical line shows the size of the Jackknife patches.

(L. Miller et al. 2013; I. Fenech Conti et al. 2017) and validated in B. Giblin et al. (2021). Photometric redshifts are calculated with self-organizing maps (H. Hildebrandt et al. 2020; A. H. Wright et al. 2020).

The Hyper Suprime-Cam (HSC) Subaru Strategic Program is conducting a 300-night *grizy* imaging survey with the 8.2 meter Subaru Telescope (H. Aihara et al. 2018). We use the 3 yr release,[14] which covers 416 deg^2 to $i < 24.5$ mag (X. Li et al. 2022). Shapes are measured with the `GalSim` (B. T. P. Rowe et al. 2015) re-Gaussianization point-spread function (PSF) correction method (C. Hirata & U. Seljak 2003). The redshift distributions are derived using the `DNNz` neural network estimator (M. M. Rau et al. 2023). We correct the mean redshifts of the HSC tomographic bins following X. Li et al. (2022) and S. Heydenreich et al. (2025).

A.2. Lensing Corrections

For each lensing survey, we correct the raw excess surface density estimator (Equation (12)) for known systematics following A. Amon et al. (2023) and S. Heydenreich et al. (2025), which we briefly outline below. In Appendix B, we report the sensitivity of our halo mass estimates to these corrections.

[14] https://hsc-release.mtk.nao.ac.jp/doc/

A.2.1. Shear Bias Corrections

The measured galaxy shapes must be calibrated to yield accurate tangential shear estimates. Shear calibration is primarily multiplicative and varies between imaging surveys. Shear calibration is applied for all of our GGL measurements.

For DES Y3, shape measurement biases are inferred by artificially shearing the observed images (METACALIBRATION; E. Huff & R. Mandelbaum 2017; E. S. Sheldon & E. M. Huff 2017; M. Gatti et al. 2021). A shear response matrix $\boldsymbol{\mathcal{R}}$ is calculated from the artificially sheared images for each galaxy:

$$\boldsymbol{\mathcal{R}}_{i,j} = \frac{\epsilon_i^{s_{j+}} - \epsilon_i^{s_{j-}}}{\Delta\gamma_j}, \tag{A1}$$

where $\epsilon_i^{s_{j+/-}}$ is the measured ellipticity of the ith component on the image positively (negatively) sheared by $\Delta\gamma_j$ in the jth component. The full response matrix is well approximated by $\mathcal{R} = (\boldsymbol{\mathcal{R}}_{11} + \boldsymbol{\mathcal{R}}_{22})/2$ (see Appendix A of M. Gatti et al. 2021). We therefore approximate the average responsivity as

$$\mathcal{R} = \frac{\sum_{i=1}^{N} w_i (\boldsymbol{\mathcal{R}}_{i,11} + \boldsymbol{\mathcal{R}}_{i,22})/2}{\sum_{i=1}^{N} w_i}, \tag{A2}$$

where w_i is the inverse-variance weight of the ith galaxy, and N is the number of galaxies. Additional biases (e.g., shear-dependent detection and blending) are calibrated by image simulations and corrected with the multiplicative biases m (N. MacCrann et al. 2022). For DES, the shear calibrated excess surface density estimator is

$$\Delta\Sigma(R) = \frac{1}{(1+m)\mathcal{R}}\Delta\Sigma_{\rm raw}(R). \tag{A3}$$

For the DES Y3 blue shear catalog, J. McCullough et al. (2024) adopted the METACALIBRATION per-galaxy response measurements and recalibrated the multiplicative bias following N. MacCrann et al. (2022).

KiDS 1000 employs a self-calibrating variant of the *lensfit* algorithm (L. Miller et al. 2013; I. Fenech Conti et al. 2017). The multiplicative bias m was calculated per tomographic bin (H. Hildebrandt et al. 2020; B. Giblin et al. 2021). For KiDS, the shear calibrated excess surface density estimator is

$$\Delta\Sigma(R) = \frac{1}{(1+m)}\Delta\Sigma_{\rm raw}(R). \tag{A4}$$

For HSC Y3, the shear responsivity is approximated as

$$\mathcal{R} = 1 - \frac{\sum_{i=1}^{N} w_i e_{i,\rm rms}^2}{\sum_{i=1}^{N} w_i}, \tag{A5}$$

where $e_{i,\rm rms}$ is the rms of the intrinsic ellipticity for the ith galaxy, and w_i is the per-galaxy inverse-variance weight (C. Hirata & U. Seljak 2003). Residual multiplicative biases are estimated as a function of signal-to-noise and resolution, using Hubble Space Telescope observations overlapping the HSC footprint (X. Li et al. 2022). We adopt the weighted average multiplicative bias across the shear catalog. HSC Y3 also corrects for multiplicative and additive biases induced by the selection criteria for sources using image simulations (S. More et al. 2023; X. Li et al. 2023). The HSC shear calibrated excess surface density estimator is then

$$\Delta\Sigma(R) = \frac{1}{1+m_{\rm sel}}\left(\frac{1}{2\mathcal{R}(1+m)}\Delta\Sigma_{\rm raw}(R) - a_{\rm sel}\Delta\Sigma^{\rm psf}\right), \tag{A6}$$

where $m_{\rm sel}$ is the multiplicative selection bias, $a_{\rm sel}$ is the additive selection bias, and $\Delta\Sigma^{\rm psf}$ is the weighted average PSF ellipticity $e^{\rm psf}$ across the source positions:

$$\Delta\Sigma^{\rm psf} = \frac{\sum_{i=1}^{N} w_i e_i^{\rm psf}}{\sum_{i=1}^{N} w_i}. \tag{A7}$$

A.2.2. Randoms Subtraction

Large-scale structure also imprints tangential shear on the source galaxies, in addition to the shear induced by the lenses. To isolate the GGL signal and account for residual additive bias, we compute the excess surface density around randomly distributed positions on the sky $\Delta\Sigma_{\rm random}$ and subtract it from the raw excess surface density estimator for the DESI lenses. For DESI, we employ the DR1 large-scale structure random catalogs. The randoms sample the area on the sky where DESI DR1 data could have been observed and reproduce the redshift distribution of the observations by randomly drawing redshifts directly from the observed data (A. J. Ross et al. 2025). We forgo the randoms correction for the eROSITA cluster measurements, because no randoms catalog is readily available. Because the overlap of the eROSITA footprint with the imaging surveys is considerably larger than for DESI (Figure 7), the contamination from large-scale structure is expected to be minor; even for DESI lenses, $\Delta\Sigma_{\rm random}$ is consistent with zero.

A.2.3. Boost Factor Correction

Because the photometric redshifts of sources are uncertain, the source redshift distribution can overlap with the lenses. Galaxies that are physically close to lenses but are erroneously identified as sources will bias the lensing signal low, particularly at small transverse separations.

To account for this bias, we multiply the raw excess surface density estimator by the boost factor $B(R)$, which estimates the amount of excess sources behind a lens compared with the random sky positions (E. S. Sheldon et al. 2004):

$$B(R) = \frac{\sum_{\rm ls} w_{\rm l} w_{\rm s}}{\sum_{\rm rs} w_{\rm r} w_{\rm s}}, \tag{A8}$$

where the numerator sums the product of the lens–source pair weights ($w_{\rm l}w_{\rm s}$), and the denominator sums the product of the random–source pair weights ($w_{\rm r}w_{\rm s}$); we again draw the randoms from the DESI DR1 randoms catalogs (A. J. Ross et al. 2025).

The boost correction is only applied for the DESI lenses, which are at higher redshift than the eROSITA lenses. For the eROSITA clusters, although the lenses are typically better separated from the sources in redshift, the cluster members are predominantly red and quenched, which increases the likelihood that cluster members are mistakenly identified as background source galaxies due to photometric redshift uncertainties. We correct for cluster lens–source contamination in Appendix B.2.

A.2.4. Lens Magnification Bias

Lensing by large-scale structure induces a (de)magnification effect on galaxy fluxes (in addition to shear). Areas of the sky with high magnification by foreground overdensities will therefore have higher number densities of detected galaxies. This connection between detection probability and large-scale structure biases excess surface density measurements: lenses are more likely to be detected if they are magnified by foreground structure, and that same structure shears the background source galaxies. We measure the magnification bias $\Delta\Sigma_{\rm mag}$ with the `dsigma` implementation of S. Unruh et al. (2020); we model the matter power spectrum with `CAMB`[15] and set $A_s = 2.83 \times 10^{-9}$. The impact of the magnification bias depends on the faint-end slope of the galaxy luminosity function α:

$$\alpha = \left.\frac{d\ln f}{d\mu}\right|_{\mu=1}, \tag{A9}$$

where f is the fraction of galaxies passing a magnitude selection, and μ is the magnification amplitude. S. Heydenreich et al.

[15] https://camb.readthedocs.io

(2025) reported α for DESI BGS and LRG in three redshift bins. We adopt $\alpha_{\rm BGS} = 2.19$ and $\alpha_{\rm LRG} = 2.52$ by interpolating the reported α at the mean redshift of the BGS and LRG samples. Following A. Amon et al. (2023), we adopt $\alpha_{\rm LOWZ} = 2.19$ and $\alpha_{\rm CMASS} = 2.52$ from M. von Wietersheim-Kramsta et al. (2021) for the SDSS samples. While the measurement of α is uncertain (e.g., Figure 15 of S. Heydenreich et al. 2025), the magnification bias correction only alters the $\Delta\Sigma$ measurement by $<2\%$ for all of the SDSS and DESI samples, corresponding to <0.01 dex in the inferred mean halo masses.

A.2.5. Measurement Covariances and Scale Cuts

We estimate the covariance matrix of the GGL measurements with a two-dimensional leave-one-out Jackknife process. For each lens sample, we divide the on-sky footprint into 100 patches via K-means clustering using `dsigma` (J. Lange & S. Huang 2022). We successively measure the excess surface density with one patch left out at a time. The mean GGL signal and the covariance matrix are then calculated from the collection of leave-one-out measurements.

The covariance matrix is only valid on angular scales smaller than the Jackknife patches (e.g., Appendix A of H. Johnston et al. 2019). For the DESI lenses, we consider three imaging surveys (DES, KiDS, and HSC). The Jackknife patches are smallest for the HSC shear catalog: $36\farcm5$ across, corresponding to 9 and 20 comoving Mpc h^{-1} at the mean redshifts of the BGS and LRG lenses, respectively. For the eROSITA lenses, we rely on the DES shear catalog because of its considerably larger overlap with the eROSITA footprint (Figure 9). The DES Jackknife patches are $110'$ across, corresponding to 14 comoving Mpc h^{-1} at $z = 0.15$ (the approximate redshift of our eROSITA lens sample).

Appendix B
Selecting a Like-for-like Simulated Sample

In this paper, we perform like-with-like comparisons between kSZ and X-ray measurements and the FLAMINGO simulations. For each sample, we identify the selection of FLAMINGO halos that best fits the measured GGL profile. We discuss the sensitivity of our results to the method of selecting simulated galaxies and corrections to the GGL for the kSZ and X-ray samples in Appendices B.1 and B.2, respectively.

B.1. SDSS and DESI kSZ Samples

For the kSZ samples, our fiducial method of selecting simulated galaxies (Section 4.2.1) is to select all galaxies above a minimum stellar mass threshold (I. G. McCarthy et al. 2025); we find the stellar mass bound that yields the best fit between the FLAMINGO $\Delta\Sigma$ profile and the observed GGL signal. This selection includes both centrals and satellites. To account for the redshift distribution of the observed sample, the simulated $\Delta\Sigma$ profile is a weighted average across the FLAMINGO redshift shells; the inferred mean halo masses change by <0.02 dex between marginalizing over the samples' redshift distributions and considering only the samples' mean redshifts. We repeat the fitting process for each FLAMINGO simulation.

To understand the robustness of the calibration, we explore multiple variations. We select galaxies in terms of halo mass, instead of stellar mass; the halo mass selection is limited to centrals, while the stellar mass cut includes both centrals and satellites. We also select galaxies from a log–normal distribution of either stellar mass or halo mass. For the log–normal selection, we fit for the central mass when calibrating to the observed GGL profile; we fix the standard deviation to 0.2 dex. For each variation of the calibration procedure, we report the mean halo mass of the selected FLAMINGO galaxies, as well as the goodness of fit between the simulation and the observed GGL and kSZ profiles; see Tables 1 and 2 for the DESI and SDSS samples, respectively. For brevity, we only report the halo masses derived from the fiducial and strongest feedback simulations. The goodness-of-fits between the simulated kSZ signals and data are weakly sensitive to the above variations.

We also investigated how sensitive the inferred halo masses are to variations in the GGL measurement. As outlined in Appendix A.2, we apply several corrections to the excess surface density measurement. The largest correction is the

Table 1
DESI GGL Calibration Summary

Name	Simulation	Satellites	Selection	Halo Mass	GGL χ^2_ν	kSZ χ^2_ν
BGS	Fiducial Feedback	✓	One sided	13.31 ± 0.008	0.67 (0.39σ)	2.18 (2.22σ)
	⋯	✓	Log–normal	13.3 ± 0.008	0.58 (0.29σ)	1.98 (2.01σ)
	⋯	⋯	One sided	13.07 ± 0.02	9.57 (6.88σ)	1.96 (1.99σ)
	⋯	⋯	Log–normal	12.98 ± 0.02	14.13 ($>10\sigma$)	1.62 (1.58σ)
	Strongest Feedback	✓	One sided	13.3 ± 0.009	0.88 (0.64σ)	1.08 (0.88σ)
	⋯	✓	Log–normal	13.3 ± 0.008	0.84 (0.6σ)	1.03 (0.82σ)
	⋯	⋯	One sided	13.09 ± 0.009	9.44 (6.82σ)	0.98 (0.76σ)
	⋯	⋯	Log–normal	12.99 ± 0.02	13.83 ($>10\sigma$)	0.89 (0.64σ)
LRG M1	Fiducial Feedback	✓	One sided	12.89 ± 0.02	1.21 (1.07σ)	0.71 (0.41σ)
	⋯	✓	Log–normal	12.89 ± 0.02	1.23 (1.09σ)	0.72 (0.42σ)
	⋯	⋯	One sided	12.66 ± 0.02	1.89 (1.97σ)	0.59 (0.27σ)
	⋯	⋯	Log–normal	12.6 ± 0.02	2.36 (2.52σ)	0.48 (0.16σ)
	Strongest Feedback	✓	One sided	12.9 ± 0.02	1.24 (1.12σ)	0.39 (0.09σ)
	⋯	✓	Log–normal	12.9 ± 0.01	1.33 (1.24σ)	0.39 (0.09σ)
	⋯	⋯	One sided	12.66 ± 0.02	1.84 (1.91σ)	0.49 (0.17σ)
	⋯	⋯	Log–normal	12.59 ± 0.02	2.23 (2.38σ)	0.55 (0.23σ)
LRG M2	Fiducial Feedback	✓	One sided	13.14 ± 0.01	2.11 (2.23σ)	4.39 (4.21σ)
	⋯	✓	Log–normal	13.13 ± 0.009	2.15 (2.29σ)	4.31 (4.15σ)
	⋯	⋯	One sided	13.0 ± 0.009	7.36 (6.5σ)	3.61 (3.59σ)

Table 1
(Continued)

Name	Simulation	Satellites	Selection	Halo Mass	GGL χ^2_ν	kSZ χ^2_ν
	⋯	⋯	Log–normal	12.91 ± 0.02	8.36 (7.08σ)	3.29 (3.31σ)
	Strongest Feedback	✓	One sided	13.13 ± 0.01	1.78 (1.83σ)	1.41 (1.33σ)
	⋯	✓	Log–normal	13.13 ± 0.01	1.85 (1.92σ)	1.45 (1.37σ)
	⋯	⋯	One sided	13.0 ± 0.009	7.01 (6.28σ)	1.3 (1.18σ)
	⋯	⋯	Log–normal	12.91 ± 0.02	8.01 (6.88σ)	1.22 (1.07σ)
LRG M3	Fiducial Feedback	✓	One sided	13.39 ± 0.009	1.33 (1.24σ)	14.1 ($>10\sigma$)
	⋯	✓	Log–normal	13.4 ± 0.008	1.45 (1.41σ)	14.06 ($>10\sigma$)
	⋯	⋯	One sided	13.28 ± 0.01	5.42 (5.22σ)	13.41 ($>10\sigma$)
	⋯	⋯	Log–normal	13.22 ± 0.01	5.96 (5.59σ)	13.38 ($>10\sigma$)
	Strongest Feedback	✓	One sided	13.39 ± 0.01	1.11 (0.93σ)	4.1 (3.99σ)
	⋯	✓	Log–normal	13.39 ± 0.008	1.1 (0.92σ)	4.5 (4.29σ)
	⋯	⋯	One sided	13.28 ± 0.01	4.58 (4.58σ)	3.63 (3.61σ)
	⋯	⋯	Log–normal	13.22 ± 0.01	5.15 (5.02σ)	3.3 (3.32σ)
LRG M4	Fiducial Feedback	✓	One sided	13.81 ± 0.01	3.58 (3.74σ)	20.39 ($>10\sigma$)
	⋯	✓	Log–normal	13.81 ± 0.01	2.84 (3.03σ)	20.08 ($>10\sigma$)
	⋯	⋯	One sided	13.76 ± 0.01	5.93 (5.58σ)	20.75 ($>10\sigma$)
	⋯	⋯	Log–normal	13.72 ± 0.01	5.98 (5.61σ)	21.12 ($>10\sigma$)
	Strongest Feedback	✓	One sided	13.81 ± 0.008	2.59 (2.77σ)	6.23 (5.48σ)
	⋯	✓	Log–normal	13.8 ± 0.01	2.06 (2.18σ)	6.86 (5.86σ)
	⋯	⋯	One sided	13.76 ± 0.01	4.71 (4.69σ)	6.01 (5.34σ)
	⋯	⋯	Log–normal	13.71 ± 0.01	4.68 (4.66σ)	6.3 (5.52σ)

Note. For each DESI kSZ sample, we report the average halo mass M_{500} inferred from the GGL FLAMINGO calibration, as well as the goodness of fit between the simulation and the observed GGL and kSZ profiles. We consider multiple variations of the GGL calibration, including (i) selecting FLAMINGO galaxies in terms of halo mass (centrals only) or stellar mass (centrals and satellites), (ii) applying a one-sided selection (all galaxies above a given mass) or selecting galaxies according to a log–normal distribution at a given central mass, and (iii) fitting to the fiducial or strongest feedback ($f_{\rm gas} - 8\sigma$) FLAMINGO simulations.

Table 2
LOWZ and CMASS GGL Calibration Summary

Name	Simulation	$n(z)$ Marginalized	Satellites	Selection	Halo Mass	GGL χ^2_ν	kSZ χ^2_ν
LOWZ	Fiducial Feedback	⋯	✓	One sided	13.5 ± 0.01	0.48 (0.12σ)	7.74 (6.37σ)
	⋯	✓	✓	One sided	13.51 ± 0.01	0.43 (0.08σ)	5.37 (4.92σ)
	⋯	⋯	✓	Log–normal	13.51 ± 0.02	0.34 (0.04σ)	9.03 (7.05σ)
	⋯	✓	✓	Log–normal	13.5 ± 0.02	0.38 (0.06σ)	6.16 (5.43σ)
	⋯	⋯	⋯	One sided	13.38 ± 0.02	1.18 (1.05σ)	11.77 ($>10\sigma$)
	⋯	✓	⋯	One sided	13.36 ± 0.02	1.37 (1.32σ)	8.18 (6.61σ)
	⋯	⋯	⋯	Log–normal	13.31 ± 0.02	1.5 (1.5σ)	12.12 ($>10\sigma$)
	⋯	✓	⋯	Log–normal	13.3 ± 0.02	1.8 (1.92σ)	8.55 (6.8σ)
	Strongest Feedback	⋯	✓	One sided	13.49 ± 0.02	0.42 (0.08σ)	1.39 (1.29σ)
	⋯	✓	✓	One sided	13.5 ± 0.01	0.49 (0.12σ)	1.11 (0.92σ)
	⋯	⋯	✓	Log–normal	13.5 ± 0.03	0.37 (0.05σ)	1.33 (1.22σ)
	⋯	✓	✓	Log–normal	13.5 ± 0.02	0.44 (0.09σ)	1.05 (0.85σ)
	⋯	⋯	⋯	One sided	13.36 ± 0.02	0.85 (0.56σ)	2.06 (2.1σ)
	⋯	✓	⋯	One sided	13.35 ± 0.02	1.02 (0.8σ)	1.44 (1.36σ)
	⋯	⋯	⋯	Log–normal	13.31 ± 0.02	1.4 (1.36σ)	1.89 (1.91σ)
	⋯	✓	⋯	Log–normal	13.29 ± 0.02	1.46 (1.45σ)	1.45 (1.37σ)
CMASS	Fiducial Feedback	⋯	✓	One sided	13.29 ± 0.02	2.45 (2.62σ)	5.46 (4.98σ)
	⋯	✓	✓	One sided	13.29 ± 0.03	2.37 (2.53σ)	5.06 (4.7σ)
	⋯	⋯	✓	Log–normal	13.27 ± 0.02	2.12 (2.25σ)	6.34 (5.54σ)
	⋯	✓	✓	Log–normal	13.28 ± 0.03	2.09 (2.21σ)	6.01 (5.33σ)
	⋯	⋯	⋯	One sided	13.16 ± 0.03	1.56 (1.55σ)	7.35 (6.14σ)
	⋯	✓	⋯	One sided	13.16 ± 0.03	1.47 (1.42σ)	7.36 (6.15σ)
	⋯	⋯	⋯	Log–normal	13.1 ± 0.03	1.42 (1.36σ)	6.92 (5.9σ)
	⋯	✓	⋯	Log–normal	13.1 ± 0.03	1.55 (1.53σ)	6.46 (5.62σ)
	Strongest Feedback	⋯	✓	One sided	13.29 ± 0.02	2.18 (2.32σ)	1.01 (0.8σ)
	⋯	✓	✓	One sided	13.29 ± 0.03	2.3 (2.45σ)	1.03 (0.83σ)
	⋯	⋯	✓	Log–normal	13.26 ± 0.03	2.29 (2.45σ)	1.09 (0.9σ)
	⋯	✓	✓	Log–normal	13.26 ± 0.03	2.29 (2.44σ)	1.07 (0.88σ)

Table 2
(Continued)

Name	Simulation	$n(z)$ Marginalized	Satellites	Selection	Halo Mass	GGL χ^2_ν	kSZ χ^2_ν
	⋯	⋯	⋯	One sided	13.13 ± 0.03	$1.29\ (1.19\sigma)$	$1.07\ (0.88\sigma)$
	⋯	✓	⋯	One sided	13.14 ± 0.03	$1.37\ (1.29\sigma)$	$1.11\ (0.92\sigma)$
	⋯	⋯	⋯	Log–normal	13.1 ± 0.03	$1.65\ (1.67\sigma)$	$1.01\ (0.8\sigma)$
	⋯	✓	⋯	Log–normal	13.1 ± 0.03	$1.53\ (1.51\sigma)$	$1.04\ (0.84\sigma)$

Note. For each SDSS galaxy sample, we report the average halo mass M_{500} inferred from the GGL FLAMINGO calibration, as well as the goodness of fit to observations. We consider the same variations to the calibration as Table 1 but include calibrations without marginalizing over the observed sample's redshift distribution $n(z)$ to facilitate comparison with I. G. McCarthy et al. (2025).

Table 3
eROSITA GGL Calibration

Redshift Selection	Halo Mass Selection $\log_{10}[M_{500}/M_\odot]$	eRASS1 Catalog	Shape Catalog	Selection	eRASS1 Mass $\log_{10}[\langle M_{500}/M_\odot\rangle]$	GGL Mass $\log_{10}[\langle M_{500}/M_\odot\rangle]$
0.05–0.1	13.3–14.0	Primary	Fiducial	One sided	13.733 ± 0.009	13.71 ± 0.1
	⋯	⋯	⋯	Log–normal	⋯	13.66 ± 0.09
	⋯	⋯	Blue shear	One sided	⋯	13.69 ± 0.12
	⋯	⋯	⋯	Log–normal	⋯	13.65 ± 0.1
	14.0–14.5	Primary	Fiducial	One sided	14.255 ± 0.004	14.19 ± 0.05
	⋯	⋯	⋯	Log–normal	⋯	14.14 ± 0.04
	⋯	⋯	Blue shear	One sided	⋯	14.14 ± 0.07
	⋯	⋯	⋯	Log–normal	⋯	14.12 ± 0.05
0.1–0.2	13.5–14.0	Primary	Fiducial	One sided	13.804 ± 0.009	13.84 ± 0.07
	⋯	⋯	⋯	Log–normal	⋯	13.78 ± 0.06
	⋯	⋯	Blue shear	One sided	⋯	13.83 ± 0.09
	⋯	⋯	⋯	Log–normal	⋯	13.77 ± 0.08
	⋯	Cosmology	Fiducial	One sided	13.844 ± 0.011	13.9 ± 0.04
	⋯	⋯	⋯	Log–normal	⋯	13.84 ± 0.08
	⋯	⋯	Blue shear	One sided	⋯	13.94 ± 0.06
	⋯	⋯	⋯	Log–normal	⋯	13.91 ± 0.1
	14.0–14.5	Primary	Fiducial	One sided	14.237 ± 0.004	14.19 ± 0.04
	⋯	⋯	⋯	Log–normal	⋯	14.16 ± 0.03
	⋯	⋯	Blue shear	One sided	⋯	14.18 ± 0.05
	⋯	⋯	⋯	Log–normal	⋯	14.15 ± 0.03
	⋯	Cosmology	Fiducial	One sided	14.247 ± 0.004	14.17 ± 0.04
	⋯	⋯	⋯	Log–normal	⋯	14.15 ± 0.03
	⋯	⋯	Blue shear	One sided	⋯	14.15 ± 0.05
	⋯	⋯	⋯	Log–normal	⋯	14.13 ± 0.03

Note. GGL derived masses for bins of eROSITA clusters. The bins are defined in terms of the reported redshift and halo mass in the eRASS1 catalogs. For the $0.1 < z < 0.2$ samples, we consider both the primary eRASS1 catalog and the higher-purity "cosmology" sample. We report the halo masses inferred from fiducial DES Y3 shear and DES Y3 blue shear. We also consider variations of the GGL fitting, including selecting FLAMINGO halos by a one-sided selection (all central halos above a given mass) or drawing halos from a log–normal distribution at a given central mass. For brevity, we only report the results using the fiducial FLAMINGO simulation.

shear bias correction; for modern lensing surveys, shape measurements are calibrated to better than 1% (e.g., A. Amon et al. 2023; X. Li et al. 2023), which corresponds to <0.005 dex uncertainty in the mean halo mass. All other corrections (randoms subtraction, boost factor, lens magnification bias) shift the GGL signal by $<10\%$ collectively (i.e., <0.05 dex in halo mass).

B.2. eROSITA Cluster Samples

For the eROSITA lens samples, our fiducial method of selecting simulated halos (Section 4.2.2) is to select all centrals above a given mass. For each bin of eROSITA clusters, we identify the minimum halo mass cutoff such that the simulated $\Delta\Sigma$ profile matches the observed GGL signal. The simulated $\Delta\Sigma$ profiles are weighted averages over the FLAMINGO lightcone redshift shells, where the weights are set by the redshift distributions of the eROSITA cluster samples.

Analogous to the kSZ samples (Appendix B.1), we explore variations of the GGL fitting process. We repeat the fit for each FLAMINGO simulation and find that the derived halo masses are insensitive to the simulation's feedback strength (<0.02 dex). Instead of selecting halos above a minimum mass, we draw halos from a log–normal distribution of halo mass. We then fit for the central mass that best reproduces the observed GGL profile; we again fix the standard deviation to 0.2 dex. For the higher-redshift bin ($z = 0.1$–0.2), we consider both the primary eRASS1 sample and the higher-purity "cosmology" sample, which requires greater detection probability (E. Bulbul et al. 2024). In Table 3, we report the derived

halo masses for each variation and find that the halo masses are insensitive to the changes (<0.05 dex). For brevity, we only report the halo masses from the fiducial feedback FLAMINGO simulation.

GGL measurements of galaxy clusters are challenged by the fact that cluster members can erroneously be included in the background source galaxy sample due to photometric redshift uncertainties, which dilutes the shear signal (H. Hoekstra et al. 2012; D. Gruen et al. 2014; J. P. Dietrich et al. 2019; T. N. Varga et al. 2019). Cluster member contamination can be modeled as a function of redshift, richness, and separation from the cluster center (e.g., S. Grandis et al. 2024b); however, these corrections require careful calibration against simulations. Instead, we adopt several strategies to minimize contamination at the data level: we restrict our analysis to larger scales (>2 comoving Mpc h^{-1}; F. Kleinebreil et al. 2025), and we repeat the GGL measurement using the blue shear catalog of J. McCullough et al. (2024). Because cluster members are predominantly red and quenched, blue galaxies are less likely to be cluster galaxies erroneously classified as background sources (I. N. Chiu et al. 2022). In Table 3, we report the derived halo masses using the fiducial DES Y3 shear catalog and the blue shear catalog. The inferred halo masses are insensitive to the choice of shear catalog (<0.05 dex change in mean halo mass).

Appendix C
Analysis of Photometric kSZ

Measurement of the kSZ effect relies upon reconstructed peculiar velocities. These velocities can be derived from spectroscopic or photometric redshifts; while photometric redshifts are more uncertain, the measured kSZ effect profile can reach comparable signal-to-noise to a spectroscopic measurement if the sample is large enough (B. Ried Guachalla et al. 2024; B. Hadzhiyska et al. 2024). In our primary analysis, we consider the spectroscopic-based kSZ measurements of E. Schaan et al. (2021) and B. Ried Guachalla et al. (2025). Complementing these measurements, B. Hadzhiyska et al. (2025b) used photometric redshifts from the DESI Legacy Imaging Survey (DR9 and DR10; R. Zhou et al. 2023a) to measure the kSZ effect for LRGs, also using the ACT DR6 map.

B. Hadzhiyska et al. (2025b) reported the photometric-based kSZ effect profile for four stellar mass bins: $\log_{10} M_*/M_\odot =$ (11, 11.25), (11.25, 11.5), (11.5, 12), and (12, 13.5). We omit the highest mass bin from our analysis, because it contains only 2000 galaxies and is potentially contaminated by the tSZ effect. We measure the GGL profile for each bin and derive a mean halo mass from the selection of simulated FLAMINGO galaxies that best fits the GGL; we use our fiducial selection function of a minimum stellar mass cut, which includes both centrals and satellites. In Figure 4, we present the amplitude of the kSZ effect profile at 2.′25 as a function of GGL derived halo mass for the spectroscopic and photometric-based kSZ measurements. Below $M_{500} = 2 \times 10^{13}\, M_\odot$, the spectroscopic and photometric kSZ measurements are both well described by the strongest feedback FLAMINGO simulation. At higher masses, the spectroscopic measurements require relatively stronger feedback than the photometric measurements. This disagreement is independent of our GGL halo masses. In Figure 9, we present the amplitude of the kSZ effect profile at 2.′25 as a function of mean stellar mass, using the photometric-based stellar masses of R. Zhou et al. (2023a). In terms of stellar mass, the spectroscopic measurements still require

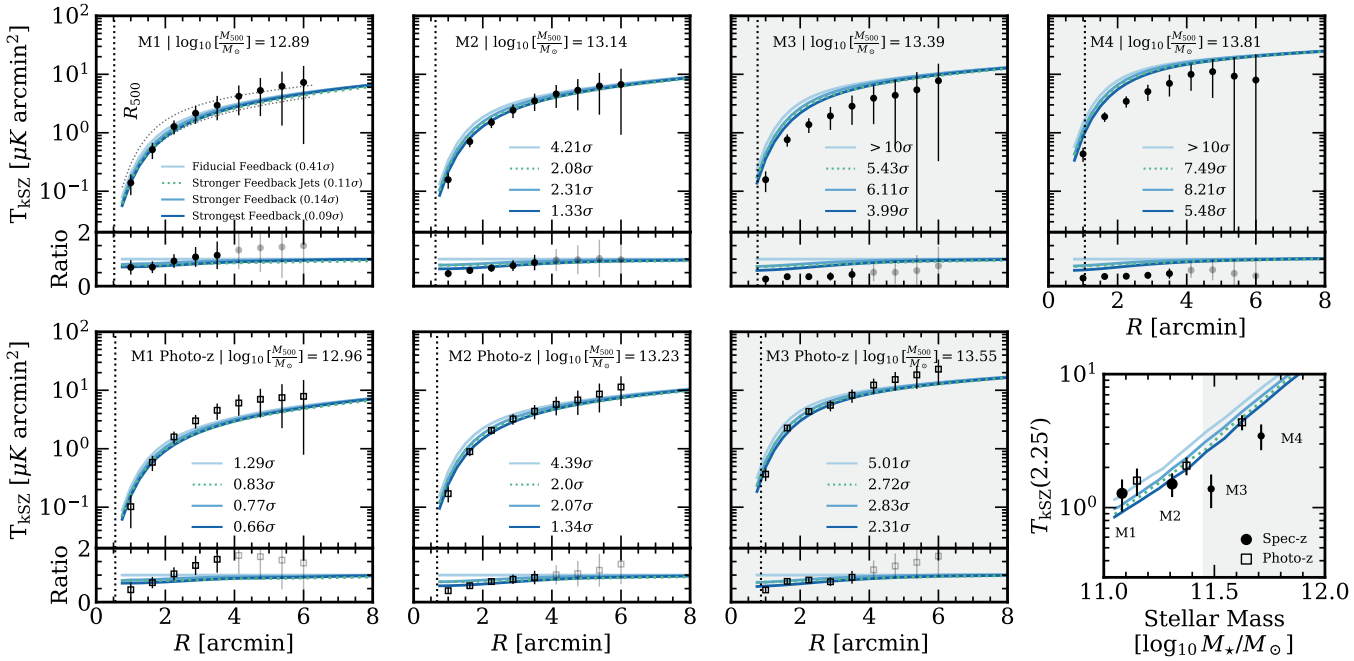

Figure 9. Comparison of the photometric (bottom) and spectroscopic (top) kSZ measurements for LRG stellar mass bins. The stacked kSZ profiles for the selection of simulated galaxies that best fits the GGL are shown for the four FLAMINGO simulations we consider. We report the number of standard deviations by which the simulation predictions deviate from the observations using the full measurement covariance matrices. The bottom panels show the ratio of the data and the simulation predictions to the fiducial simulation. The vertical dotted line demarcates R_{500}. The kSZ effect measurement is highly correlated at larger angular separations, so these bins carry lower statistical weight. The bottom-right panel presents the amplitude of the stacked kSZ effect at $\theta = 2.25'$ for the spectroscopic (B. Ried Guachalla et al. 2025) and photometric (B. Hadzhiyska et al. 2024) LRG mass bins as a function of mean stellar mass (R. Zhou et al. 2023a), alongside the simulation predictions. At $M_\star > 2.5 \times 10^{11}\, M_\odot$ (shaded gray), the spectroscopic and photometric results require different feedback strengths.

stronger feedback than the photometric measurements for the highest-mass bins.

The kSZ amplitude versus halo-mass relation neglects the full shape of the kSZ effect profile. We therefore perform our like-with-like analysis on the photometric-based kSZ profiles. For each stellar mass bin, we calculate the stacked kSZ effect profile from the selection of simulated galaxies that best fits the GGL measurements; following our primary analysis, we marginalize over the redshift distribution of each stellar mass bin. The simulation predictions are presented against the data in Figure 9. We also present the like-with-like comparison for all four spectroscopic-based LRG kSZ bins. In Figure 9, we report the number of standard deviations between the data and the simulation predictions using the full kSZ covariance matrices. Our simulation comparison finds that the photometric kSZ measurements are well described by the strongest feedback FLAMINGO simulation ($f_{\rm gas}\ -\ 8\sigma$) for all mass bins, as are the two lowest-mass bins of the spectroscopic measurements (M1 and M2). However, the two highest-mass spectroscopic bins (M3 and M4) appear to require even stronger feedback than the photometric measurements.

Given the differences between the spectroscopic- and photometric-based kSZ measurements, we omit the highest-mass LRG bins from our primary analysis. Both the spectroscopic and photometric measurements require stronger feedback than the fiducial FLAMINGO simulation, but they differ on whether even stronger feedback than $f_{\rm gas}\ -\ 8\sigma$ is required. Future work is necessary to understand this result, including an investigation of observational uncertainties and potential systematics in how we match with simulations.

ORCID iDs

Jared C. Siegel https://orcid.org/0000-0002-9337-0902
Alexandra Amon https://orcid.org/0000-0002-6445-0559
Ian G. McCarthy https://orcid.org/0000-0002-1286-483X
Leah Bigwood https://orcid.org/0000-0002-9870-3331
Masaya Yamamoto https://orcid.org/0000-0003-1585-997X
Esra Bulbul https://orcid.org/0000-0002-7619-5399
Jenny E. Greene https://orcid.org/0000-0002-5612-3427
Jamie McCullough https://orcid.org/0000-0002-4475-3456
Matthieu Schaller https://orcid.org/0000-0002-2395-4902
Joop Schaye https://orcid.org/0000-0002-0668-5560

References

Abbott, T. M. C., Aguena, M., Alarcon, A., et al. 2022, PhRvD, 105, 023520
Adame, A. G., Aguilar, J., Ahlen, S., et al. 2025a, JCAP, 2025, 017
Adame, A. G., Aguilar, J., Ahlen, S., et al. 2025b, JCAP, 2025, 012
Ahn, C. P., Alexandroff, R., Allende Prieto, C., et al. 2012, ApJS, 203, 21
Ahn, C. P., Alexandroff, R., Allende Prieto, C., et al. 2014, ApJS, 211, 17
Aihara, H., Arimoto, N., Armstrong, R., et al. 2018, PASJ, 70, S4
Akeson, R., Armus, L., Bachelet, E., et al. 2019, arXiv:1902.05569
Akino, D., Eckert, D., Okabe, N., et al. 2022, PASJ, 74, 175
Amon, A., & Efstathiou, G. 2022, MNRAS, 516, 5355
Amon, A., Robertson, N. C., Miyatake, H., et al. 2023, MNRAS, 518, 477
Bahar, Y. E., Bulbul, E., Ghirardini, V., et al. 2024, A&A, 691, A188
Battaglia, N., Ferraro, S., Schaan, E., & Spergel, D. N. 2017, JCAP, 2017, 040
Bigwood, L., Amon, A., Schneider, A., et al. 2024, MNRAS, 534, 655
Bigwood, L., Bourne, M. A., Iršič, V., Amon, A., & Sijacki, D. 2025a, MNRAS, 542, 3206
Bigwood, L., Yamamoto, M., Siegel, J., et al. 2025b, arXiv:2510.15822
Booth, C. M., & Schaye, J. 2009, MNRAS, 398, 53
Braspenning, J., Schaye, J., Schaller, M., Kugel, R., & Kay, S. T. 2025, MNRAS, 536, 3784
Braspenning, J., Schaye, J., Schaller, M., et al. 2024, MNRAS, 533, 2656
Bulbul, E., Liu, A., Kluge, M., et al. 2024, A&A, 685, A106
Bulbul, G. E., Smith, R. K., Foster, A., et al. 2012, ApJ, 747, 32
Bundy, K., Leauthaud, A., Saito, S., et al. 2015, ApJS, 221, 15
Chisari, N. E., Mead, A. J., Joudaki, S., et al. 2019, OJAp, 2, 4
Chiu, I. N., Ghirardini, V., Liu, A., et al. 2022, A&A, 661, A11
Choi, E., Ostriker, J. P., Naab, T., & Johansson, P. H. 2012, ApJ, 754, 125
Clerc, N., Comparat, J., Seppi, R., et al. 2024, A&A, 687, A238
Conroy, C., & Ostriker, J. P. 2008, ApJ, 681, 151
Coulton, W., Madhavacheril, M. S., Duivenvoorden, A. J., et al. 2024, PhRvD, 109, 063530
Dalal, N., To, C.-H., Hirata, C., et al. 2026, JCAP, 2026, 036
Dalla Vecchia, C., & Schaye, J. 2012, MNRAS, 426, 140
de Jong, J. T. A., Kuijken, K., Applegate, D., et al. 2013, Msngr, 154, 44
Debackere, S. N. B., Schaye, J., & Hoekstra, H. 2020, MNRAS, 492, 2285
Dietrich, J. P., Bocquet, S., Schrabback, T., et al. 2019, MNRAS, 483, 2871
Driver, S. P., Bellstedt, S., Robotham, A. S. G., et al. 2022, MNRAS, 513, 439
Eckert, D., Ettori, S., Coupon, J., et al. 2016, A&A, 592, A12
Eckert, D., Gaspari, M., Gastaldello, F., Le Brun, A. M. C., & O'Sullivan, E. 2021, Univ, 7, 142
Eckert, D., Ghirardini, V., Ettori, S., et al. 2019, A&A, 621, A40
Eckert, D., Seppi, R., Braspenning, J., et al. 2026, A&A, 709, L4
Eisenstein, D. J., Seo, H.-J., Sirko, E., & Spergel, D. N. 2007, ApJ, 664, 675
Euclid Collaboration, Mellier, Y., Abdurro'uf, et al. 2025, A&A, 697, A1
Fabian, A. C. 2012, ARA&A, 50, 455
Fenech Conti, I., Herbonnet, R., Hoekstra, H., et al. 2017, MNRAS, 467, 1627
Fowler, J. W., Niemack, M. D., Dicker, S. R., et al. 2007, ApOpt, 46, 3444
Gaspari, M., Tombesi, F., & Cappi, M. 2020, NatAs, 4, 10
Gatti, M., Sheldon, E., Amon, A., et al. 2021, MNRAS, 504, 4312
Ghirardini, V., Bulbul, E., Artis, E., et al. 2024, A&A, 689, A298
Giblin, B., Heymans, C., Asgari, M., et al. 2021, A&A, 645, A105
Giri, S. K., & Schneider, A. 2021, JCAP, 2021, 046
Gitti, M., Brighenti, F., & McNamara, B. R. 2012, AdAst, 2012, 950641
Gonzalez, A. H., Sivanandam, S., Zabludoff, A. I., & Zaritsky, D. 2013, ApJ, 778, 14
Górski, K. M., Hivon, E., Banday, A. J., et al. 2005, ApJ, 622, 759
Grandis, S., Aricò, G., Schneider, A., & Linke, L. 2024a, MNRAS, 528, 4379
Grandis, S., Ghirardini, V., Bocquet, S., et al. 2024b, A&A, 687, A178
Gruen, D., Seitz, S., Brimioulle, F., et al. 2014, MNRAS, 442, 1507
Hadzhiyska, B., Ferraro, S., Farren, G. S., Sailer, N., & Zhou, R. 2025a, PhRvD, 112, 123507
Hadzhiyska, B., Ferraro, S., Ried Guachalla, B., & Schaan, E. 2024, PhRvD, 109, 103534
Hadzhiyska, B., Ferraro, S., Ried Guachalla, B., et al. 2025b, PhRvD, 112, 083509
Hahn, C., Wilson, M. J., Ruiz-Macias, O., et al. 2023, AJ, 165, 253
Heckman, T. M., & Best, P. N. 2014, ARA&A, 52, 589
Henden, N. A., Puchwein, E., Shen, S., & Sijacki, D. 2018, MNRAS, 479, 5385
Henderson, S. W., Allison, R., Austermann, J., et al. 2016, JLTP, 184, 772
Heydenreich, S., Leauthaud, A., Blake, C., et al. 2025, arXiv:2506.21677
Hildebrandt, H., Köhlinger, F., van den Busch, J. L., et al. 2020, A&A, 633, A69
Hirata, C., & Seljak, U. 2003, MNRAS, 343, 459
Hoekstra, H., Herbonnet, R., Muzzin, A., et al. 2015, MNRAS, 449, 685
Hoekstra, H., Mahdavi, A., Babul, A., & Bildfell, C. 2012, MNRAS, 427, 1298
Hopkins, P. F., Silich, E., Sayers, J., Ponnada, S. B., & Sands, I. 2026, arXiv:2601.22229
Huff, E., & Mandelbaum, R. 2017, arXiv:1702.02600
Huško, F., Lacey, C. G., Schaye, J., Schaller, M., & Nobels, F. S. J. 2022, MNRAS, 516, 3750
Ivezić, Ž., Kahn, S. M., Tyson, J. A., et al. 2019, ApJ, 873, 111
Johnston, H., Georgiou, C., Joachimi, B., et al. 2019, A&A, 624, A30
Kleinebreil, F., Grandis, S., Schrabback, T., et al. 2025, A&A, 695, A216
Kluge, M., Comparat, J., Liu, A., et al. 2024, A&A, 688, A210
Kormendy, J., & Ho, L. C. 2013, ARA&A, 51, 511
Kovač, M., Nicola, A., Bucko, J., et al. 2025, JCAP, 2025, 046
Kravtsov, A. V., Vikhlinin, A. A., & Meshcheryakov, A. V. 2018, AstL, 44, 8
Kugel, R., Schaye, J., Schaller, M., et al. 2023, MNRAS, 526, 6103
Kuijken, K., Heymans, C., Dvornik, A., et al. 2019, A&A, 625, A2
La Posta, A., Alonso, D., Chisari, N. E., Ferreira, T., & García-García, C. 2025, PhRvD, 112, 043525
Laganá, T. F., Martinet, N., Durret, F., et al. 2013, A&A, 555, A66
Lange, J., & Huang, S. 2022, dsigma: Galaxy-galaxy lensing Python package, Astrophysics Source Code Library, ascl:2204.006

Lange, J. U., Blake, C., Saulder, C., et al. 2024, OJAp, 7, 57
Li, X., Miyatake, H., Luo, W., et al. 2022, PASJ, 74, 421
Li, X., Zhang, T., Sugiyama, S., et al. 2023, PhRvD, 108, 123518
Lin, Y.-T., Stanford, S. A., Eisenhardt, P. R. M., et al. 2012, ApJL, 745, L3
Liu, A., Bulbul, E., Ghirardini, V., et al. 2022, A&A, 661, A2
Liu, R. H., Ferraro, S., Schaan, E., et al. 2025, PhRvD, 112, 083561
Lovisari, L., Reiprich, T. H., & Schellenberger, G. 2015, A&A, 573, A118
Lovisari, L., Schellenberger, G., Sereno, M., et al. 2020, ApJ, 892, 102
MacCrann, N., Becker, M. R., McCullough, J., et al. 2022, MNRAS, 509, 3371
Mallaby-Kay, M., Amodeo, S., Hill, J., et al. 2023, PhRvD, 108, 023516
Manera, M., Samushia, L., Tojeiro, R., et al. 2015, MNRAS, 447, 437
Manera, M., Scoccimarro, R., Percival, W. J., et al. 2013, MNRAS, 428, 1036
Marini, I., Popesso, P., Dolag, K., et al. 2025, A&A, 694, A207
Marini, I., Popesso, P., Lamer, G., et al. 2024, A&A, 689, A7
Maughan, B. J., Jones, C., Forman, W., & Van Speybroeck, L. 2008, ApJS, 174, 117
McCarthy, I. G., Amon, A., Schaye, J., et al. 2025, MNRAS, 540, 143
McCarthy, I. G., Bird, S., Schaye, J., et al. 2018, MNRAS, 476, 2999
McCarthy, I. G., Schaye, J., Bird, S., & Le Brun, A. M. C. 2017, MNRAS, 465, 2936
McCarthy, I. G., Schaye, J., Bower, R. G., et al. 2011, MNRAS, 412, 1965
McCullough, J., Amon, A., Legnani, E., et al. 2024, arXiv:2410.22272
McNamara, B. R., & Nulsen, P. E. J. 2007, ARA&A, 45, 117
Merloni, A., Lamer, G., Liu, T., et al. 2024, A&A, 682, A34
Miller, L., Heymans, C., Kitching, T. D., et al. 2013, MNRAS, 429, 2858
More, S., Sugiyama, S., Miyatake, H., et al. 2023, PhRvD, 108, 123520
Moustakas, J., Buhler, J., Scholte, D., Dey, B., & Khederlarian, A. 2023, FastSpecFit: Fast spectral synthesis and emission-line fitting of DESI spectra, Astrophysics Source Code Library, ascl:2308.005
Muñoz-Echeverría, M., Macías-Pérez, J. F., Pratt, G. W., et al. 2024, A&A, 682, A147
Mulroy, S. L., Farahi, A., Evrard, A. E., et al. 2019, MNRAS, 484, 60
Myles, J., Alarcon, A., Amon, A., et al. 2021, MNRAS, 505, 4249
Naess, S., Guan, Y., Duivenvoorden, A. J., et al. 2025, JCAP, 2025, 061
Nandra, K., Barret, D., Barcons, X., et al. 2013, arXiv:1306.2307
Okabe, N., Reiprich, T. H., Grandis, S., et al. 2025, A&A, 700, A46
Pakmor, R., Springel, V., Coles, J. P., et al. 2023, MNRAS, 524, 2539
Pandey, S., Hill, J. C., Alarcon, A., et al. 2025, arXiv:2506.07432
Pearson, R. J., Ponman, T. J., Norberg, P., et al. 2017, MNRAS, 469, 3489
Planck Collaboration, Aghanim, N., Akrami, Y., et al. 2020, A&A, 641, A1
Popesso, P., Biviano, A., Bulbul, E., et al. 2024, MNRAS, 527, 895
Popesso, P., Biviano, A., Marini, I., et al. 2026, A&A, 707, A362
Pratt, G. W., Arnaud, M., Piffaretti, R., et al. 2010, A&A, 511, A85
Predehl, P., Andritschke, R., Arefiev, V., et al. 2021, A&A, 647, A1
Preston, C., Amon, A., & Efstathiou, G. 2023, MNRAS, 525, 5554
Quataert, E., & Hopkins, P. F. 2025, OJAp, 8, 66
Rasmussen, J., & Ponman, T. J. 2009, MNRAS, 399, 239
Rau, M. M., Dalal, R., Zhang, T., et al. 2023, MNRAS, 524, 5109
Reischke, R., & Hagstotz, S. 2025, arXiv:2507.17742
Ried Guachalla, B., Schaan, E., Hadzhiyska, B., & Ferraro, S. 2024, PhRvD, 109, 103533
Ried Guachalla, B., Schaan, E., Hadzhiyska, B., et al. 2025, PhRvD, 112, 103512
Robotham, A. S. G., Norberg, P., Driver, S. P., et al. 2011, MNRAS, 416, 2640
Ross, A. J., Aguilar, J., Ahlen, S., et al. 2025, JCAP, 2025, 125
Rowe, B. T. P., Jarvis, M., Mandelbaum, R., et al. 2015, A&C, 10, 121
Rykoff, E. S., Rozo, E., Busha, M. T., et al. 2014, ApJ, 785, 104
Rykoff, E. S., Rozo, E., Hollowood, D., et al. 2016, ApJS, 224, 1
Salcido, J., McCarthy, I. G., Kwan, J., Upadhye, A., & Font, A. S. 2023, MNRAS, 523, 2247
Sanders, J. S., Fabian, A. C., Russell, H. R., & Walker, S. A. 2018, MNRAS, 474, 1065
Sanderson, A. J. R., O'Sullivan, E., Ponman, T. J., et al. 2013, MNRAS, 429, 3288
Schaan, E., Ferraro, S., Vargas-Magaña, M., et al. 2016, PhRvD, 93, 082002
Schaan, E., Ferraro, S., Amodeo, S., et al. 2021, PhRvD, 103, 063513
Schaye, J., Crain, R. A., Bower, R. G., et al. 2015, MNRAS, 446, 521
Schaye, J., Kugel, R., Schaller, M., et al. 2023, MNRAS, 526, 4978
Schneider, A., Giri, S. K., Amodeo, S., & Refregier, A. 2022, MNRAS, 514, 3802
Seppi, R., Comparat, J., Bulbul, E., et al. 2022, A&A, 665, A78
Seppi, R., Eckert, D., Finoguenov, A., et al. 2025, A&A, 699, A206
Sevilla-Noarbe, I., Bechtol, K., Carrasco Kind, M., et al. 2021, ApJS, 254, 24
Sheldon, E. S., & Huff, E. M. 2017, ApJ, 841, 24
Sheldon, E. S., Johnston, D. E., Frieman, J. A., et al. 2004, AJ, 127, 2544
Silk, J., & Rees, M. J. 1998, A&A, 331, L1
Siudek, M., Pucha, R., Mezcua, M., et al. 2024, A&A, 691, A308
Springel, V., Di Matteo, T., & Hernquist, L. 2005, ApJL, 620, L79
Sun, M., Voit, G. M., Donahue, M., et al. 2009, ApJ, 693, 1142
Sunyaev, R., Arefiev, V., Babyshkin, V., et al. 2021, A&A, 656, A132
Sunyaev, R. A., & Zeldovich, Y. B. 1972, CoASP, 4, 173
Sunyaev, R. A., & Zeldovich, Y. B. 1980, MNRAS, 190, 413
Swetz, D. S., Ade, P. A. R., Amiri, M., et al. 2011, ApJS, 194, 41
The Dark Energy Survey Collaboration 2005, arXiv:astro-ph/0510346
Thornton, R. J., Ade, P. A. R., Aiola, S., et al. 2016, ApJS, 227, 21
Truemper, J. 1982, AdSpR, 2, 241
Unruh, S., Schneider, P., Hilbert, S., et al. 2020, A&A, 638, A96
van Daalen, M. P., McCarthy, I. G., & Schaye, J. 2020, MNRAS, 491, 2424
van Daalen, M. P., Schaye, J., Booth, C. M., & Dalla Vecchia, C. 2011, MNRAS, 415, 3649
Varga, T. N., DeRose, J., Gruen, D., et al. 2019, MNRAS, 489, 2511
Velliscig, M., van Daalen, M. P., Schaye, J., et al. 2014, MNRAS, 442, 2641
Vikhlinin, A., Kravtsov, A., Forman, W., et al. 2006, ApJ, 640, 691
Voges, W., Aschenbach, B., Boller, T., et al. 1999, A&A, 349, 389
von Wietersheim-Kramsta, M., Joachimi, B., van den Busch, J. L., et al. 2021, MNRAS, 504, 1452
White, M. 2015, MNRAS, 450, 3822
Wright, A. H., Hildebrandt, H., van den Busch, J. L., & Heymans, C. 2020, A&A, 637, A100
Zhou, R., Dey, B., Newman, J. A., et al. 2023a, AJ, 165, 58
Zhou, R., Ferraro, S., White, M., et al. 2023b, JCAP, 2023, 097